Original Paper

Multiscale characterization of the Albian-Cenomanian reservoir system behavior: A case study from the North East Abu Gharadig Basin, North Western Desert, Egypt

Ola Rashad [a, *], Ahmed Niazy El-Barkooky [a], Abd El-Moneim El-Araby [a], Mohamed El-Tonbary [b]

[a] Geology Department, Faculty of Science, Cairo University, Giza Governorate, 12613, Egypt
[b] Capricorn Energy-Bapetco Joint Venture, Western Desert, Egypt

ARTICLE INFO

ABSTRACT

Since its discovery in 2010, the NEAG 2 has been one of the most productive oil fields of the Badr El-Din Petroleum Company (BAPETCO) in the northern Western Desert of Egypt. The Albian-Cenomanian reservoir system has a unique performance but suffers from several issues hindering its production. The latest production report in 2023, NEAG-2 Field was producing 1760 bbls of oil with 36500 bbls of water, i.e., 95% water cut. Despite that, the field has reached a 39% recovery factor but the reservoir forecast suggests a much higher recovery factor. Therefore, the NEAG 2 Field requires a comprehensive geological model to depict its reservoir heterogeneities better. We introduce a solid and integrated workflow to investigate the reservoir characters among different scales of geological heterogeneity and offer solutions to overcome some data gaps. After characterizing the reservoir elements by the structural, stratigraphic, petrographic, and petrophysical analyses, a machine learning-based method was applied to overcome the missing whole rock cores in creating a detailed electro-facies log for all field wells. The Neural-Network algorithm required the facies types to be grouped into definitive reservoir qualities to be applied. The resultant electro-facies log had a very good match with the input logs, which validated the facies grouping. This was followed by the porosity-permeability transforms, estimated from mobility data, to create a permeability curve for all field wells, despite the unavailability of core data. The reservoir was categorized into three rock types, each with a specific range of quality, signifying their different flow abilities which were supported by dynamic data. The Lower Bahariya-Kharita in NEAG 2 was ultimately concluded to be a complex heterogeneous reservoir with varying flow abilities and production behaviors. The recovery factor mismatch is due to unrecovered reserves, and a new production strategy should be introduced to reach the ultimate recovery. This integration of geologic and dynamic data is strongly recommended for any reservoir characterization study to avoid oversimplifying the reservoir system and to design the right reservoir development plan.

1. Introduction

Reservoir heterogeneity is characterized by various types and scales, from the largest to the smallest scale; they are megascopic, macroscopic, mesoscopic, and microscopic heterogeneities (Krause et al., 1987). To accurately predict the fluid flow within a reservoir, the variability in the rock properties relevant to the specific depositional environment needed to be considered at all scales (Schatzinger and Tomutsa, 1999). The unavailability and ignorance of some data lead to knowledge gaps and reservoir misrepresentation. However, if all available datasets are properly integrated to build a comprehensive and detailed geologic model for these heterogeneous reservoirs, better strategies will be designed to optimize field productions. An example from the North East Abu Gharadig (NEAG) area in the North Western Desert province in Egypt will be described to show how geologic data should be integrated and guided by the actual production data. In this way, the geological uncertainties of the created model will be constrained by

* Corresponding author.
E-mail address: Orashad@sci.cu.edu.eg (O. Rashad).

the real dynamic data (pressure and production rates), to solve the field issues and optimize its production. The Bahariya reservoir was studied previously in many other fields and was concluded to be a heterogeneous reservoir in terms of flow properties (Farrag et al., 2021). Others studied the core samples of the Bahariya Formation and defined 2 RRTs, that exhibit an extremely heterogeneous nature (El Hossainy et al., 2021). Some other studies revealed the good textural maturity of the Bahariya sandstones and the promising petrophysical characteristics of low shale volume and high effective porosity ranges between 10 and 20% (Shehata and Sarhan, 2022).

NEAG 2 Field is a brown field with excellent production performance and economic value; it was one of the main contributors to Bapetco liquid production in 2016 (Rashad et al., 2022). Currently, the field suffers many production issues and geologic uncertainties that need to be handled and mitigated. In dealing with such an economic reservoir, all sorts of data and facts should be considered. The problem statement of NEAG 2 Field is the unexpected high water cut and the declining oil production rate. The main question is whether the field is reaching its final destination (ceasing to flow) or whether there is still some potential. Considering the fact that the current recovery factor (RF) is much lower than the predicted one based on the Top Quartile (TQ) analysis. Was the previously calculated STOIIP overestimating the reserve, or the TQ RF was inaccurate? How would the reservoir characterization approach and integration of different workflows change the game? How far would this study help leverage the remaining value of the field? By the end of this research, these paradoxes will be resolved, and a new vision will be introduced for NEAG 2 Field.

This research aims to study the elements of reservoir heterogeneity at different scales and describes their effect on reservoir behavior. Investigating the heterogeneity from production data will improve the predictions, the pressure data validates and supports the stratigraphic and geologic complexity of the reservoir (Stearman, 2023). The geological elements that control the reservoir's system behavior are mineralogy, grain size, packing, pore network, lithohydraulic units, lithologic continuity, fractures and faults, and rock-fluid interactions. Each one of those elements represents a different scale of heterogeneity. Therefore, the Lower Bahariya-Kharita Reservoir in NEAG 2 Field will be described in four scales of heterogeneities: (1) Megascale, the field-wide view; (2) Macro-scale, the inter-well lateral continuity; (3) Meso-scale, the surroundings of the well; and (4) Micro-scale, the domain of grains and pores, following the workflow done by Krause et al. (1987). In previous work by Rashad et al. (2022), a seismic inversion workflow differentiated the reservoir distribution trends, describing its megascale heterogeneities as a preliminary phase. In that work, different seismic inversion techniques were applied to resolve the reservoir with diverse bodies' geometries and dimensions. The reservoir was resolved as widely extended sheets, channelised, and small lobes of sand. The trends of the reservoir distribution were not clearly defined, referring to the diverse geometries of the reservoir bodies (Rashad et al., 2022).

The hierarchy followed in the current reservoir multiscale anatomy will be described from the largest scale to the smallest. The integrated workflow began with the macroscopic or field-scale heterogeneities aroused from structural elements (faults and fractures) and stratigraphic relations. Then mesoscopic or well-scale heterogeneities were recognised from image logs. These were followed by the petrographic analysis that provided the microscopic or pore/grain-scale heterogeneities. The reservoir system characterization was accomplished by defining flow units, components, and drive mechanisms.

Some of the interpretations from the service companies' reports were utilized as input in the created workflows, each used report was cited in the text as SENV (2009); Halliburton (2011);

Halliburton (2015); EREX (2015); Schlumberger (2015a); Schlumberger (2015b); and Corex (2019). Other than that, all of the described results are produced from the current research work, by the current authors.

2. Field background

NEAG 2 lies within the eastern part of the North East Abu El-Gharadig (NEAG) Extension concession in the northern Western Desert of Egypt (Fig. 1). NEAG 2 Field is in East Abu Gharadig Basin near Mubarak Inversion as in (Fig. 1). NEAG 1 Field occupied Mubarak Arc that has the same reservoir interval, but at nearly 1 Km shallower. Abu Gharadig Basin has isolated from the North East Abu Gharadig (NEAG) area by the Mubarak Arch anticline. The East Abu Gharadig Basin (1000 km^2) can be described as a mini basin with the larger Abu Gharadig Basin (Fahmy et al., 2018). In the mid-Turonian-Santonian time, in the East Abu Gharadig Basin, a high area was developed between two opposing half-graben depocenters that were controlled by basin margin faults. The absence of mid-Turonian inversion in the Abu Gharadig Basin could be due to the absence of NE-SW striking faults, which have an orientation suitable for pop-up development (Sarhan and Collier, 2018).

However, the structural setting and stratigraphic sequences of the Abu Gharadig Basin are the same in the NEAG area. Some of the shallow formations were eroded or deposited with variable thicknesses, due to the Late Cretaceous inversion (El Gazzar et al., 2016). NEAG 2 Field is located at 127 km distance from Cairo (Fig. 1) and extends into 8 km in E-W direction and 3.7 km in N-S direction between Latitude 29°54′ to 29°52′N and Longitude 29°50′60″ to 29°56′E (SENV, 2008).

Several reservoir rocks are found in the Abu Gharadig Basin, the deepest reservoir is the Albian Kharita Formation, Cenomanian Bahariya Formation, to the shallowest Abu Roash G, E, and C members and with a limited extent Apollonia Formation of the Paleocene-Eocene age. In The East Abu Gharadig Basin, only the Kharita-Bahariya reservoir system is producing. The Lower Cenomanian reservoirs of the Bahariya Formation are the main reservoirs in the NEAG basin (Fahmy et al., 2023). Regarding the hydrocarbon charge, the Jurassic Khatatba source rock offers the best chance of charge for the eastern NEAG Extension area. The Abu Roash F Member, which is the main source rock within the central Abu Gharadig Basin, is immature in the east.

In the NEAG 2 Field, ten wells were drilled but only four producers are still opened out of eight producer wells. The field production has some issues; the overwhelming problem is handling the massive amount of water produced from each well. Currently, the field is producing from the 4 wells with an average daily rate of 1700 bbl of oil with 36000 bbls of water, which is >95% water cut. The field showed different production behaviors from different reservoir zones regarding the production history. This behavior is associated with unexpected water production, variable drainage ability from different stratigraphic levels, and fluctuating waterfront. Moreover, the pressure regime is not the same among different field segments. The same reservoir section especially the Bahariya had been concluded to be heterogeneous with a higher degree of complexity relative to the Lower units of the Kharita reservoir by Farouk et al. (2021) and many other literature.

In 2018, the west segment in the field was reported with STOIIP = 40MMstb, and cumulative oil production = 15.7, with a recovery factor (RF) = 39%; however, the estimated recovery factor is (RF) > 55 %. The mismatch between the actual and the estimated RFs indicated that the reservoir system is not clearly understood and that there is a gap in reaching the Top Quartile Recovery Factor (TQ RF). The TQ RF analysis is delivered from the Reservoir
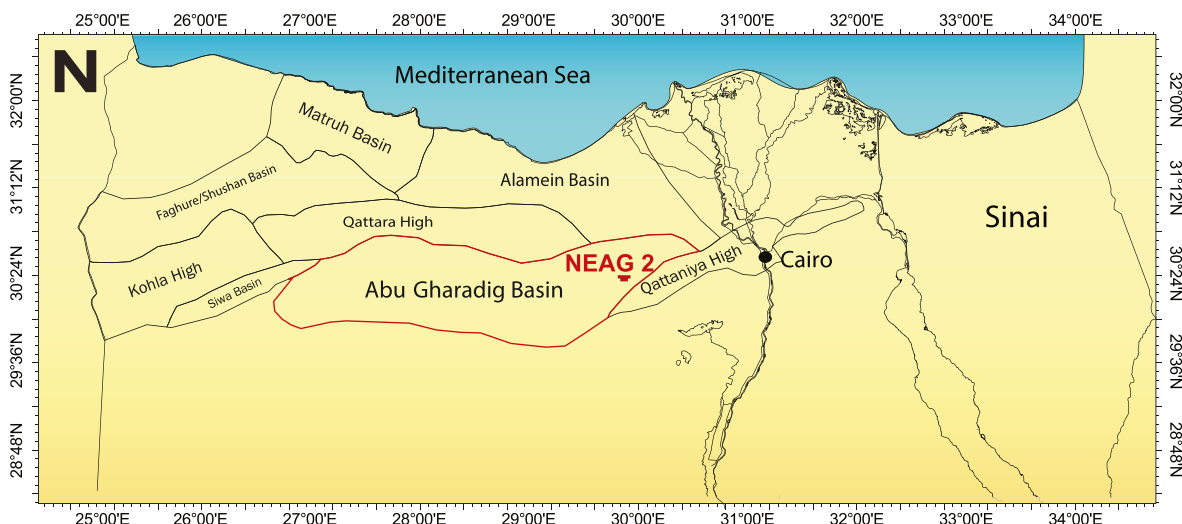
Fig. 1. Abu El Gharadig Basin location map in the north Western Desert of Egypt. The NEAG-2 Field concession is colored in red, located in the North-Eastern part of Abu El Gharadig Basin (NEAG).

Performance Reviews (RPR). Shell Company created the Top Quartile Estimated Ultimate Recovery (TQ EUR) tool as a benchmarking tool to identify the maximum estimated recovery potential for the field (Prelicz et al., 2014). The RPRs tool integrates reservoir knowledge, hydrocarbon saturations, and production data to identify opportunities, restoration, acceleration, and reserves addition. These predictions are based on dynamic simulations with reservoir models that have been historically matched for each field area (Prelicz et al., 2014). After a complexity factor is calculated, it can be translated into a Top Quartile Recovery Factor (TQ RF), and then the gap to the TQ recovery is identified, i.e., the remaining volumes. This means that the geologic data should be integrated and guided by the dynamic data in the reservoir characterization workflow. By the end of this paper, the RF mismatch will be concluded as overestimated calculated oil volumes or unrecoverable reserves.

3. Database and methodology

Conventional well logs such as Gamma-ray (GR), Density (DEN), Neutron (NEU), Resistivity (RES), Photoelectric factor (PEF), and Caliper (CAL) were acquired in all field wells. In addition to some advanced logs such as the Cement logs and Thermal decay time (TDT) logs. Using GR, DEN/NEU logs, the NTG, PorNet, and S_{HC} logs were calculated by the Bapetco Petrophysics Team for the field petrophysical evaluation. Furthermore, the formation pressure data were acquired in most field wells (Table 1), and the fluid sample was acquired only in the exploration Well NEAG 2-1.

In NEAG 2, various BHI tools were used; OMRI was acquired in the NEAG 2-E1 well, FMI in the NEAG2-5 well, and XRMI in the NEAG 2-4st well. The different image logs offered qualitative and quantitative descriptions for the reservoir facies, structural dip, faults, and fracture analysis, as reported by Schlumberger (2015a), Halliburton (2011), and Halliburton (2015). NEAG 2 Field data limitation is mainly the lack of whole-rock cores. The availability of core data would have provided a good opportunity to cross-check the BHI interpretations with rock descriptions and petrographic analysis of the core data, as in the work done by Samantray et al. (2010). The absence of a whole rock core has been an obstacle in understanding the reservoir architecture, lithofacies, or sedimentary structures besides the inability to measure permeability or saturation directly from real data. However, these constraints were

compensated by some other pieces of data. As an alternative, dich-cutting petrographic analysis validated the BHI interpretation. We present in this paper a very good example of data compensation in some wells by applying the neural network (machine learning-based) method to get the learnings from the control points and apply them to those with less data. The ditch-cutting analysis was conducted in NGAG 2-1, NEAG 2-4St, NEAG 2-6, and NEAG 2-E1 by SENV (2009) and Corex (2019). Petrography analysis was performed on these wells except for NEAG 2-1. Chronology and biostratigraphy were performed on NEAG 2-1 and NEAG 2-4St wells by SENV (2009) and EREX (2015), respectively.

According to the data available in the field, key wells with the best data were selected to represent the reservoir (Table 1). Limited by the available data and to overcome the gaps, different key wells were used as control points in different modules. All key wells from each analysis were integrated and contrasted with those with fewer data to complete the reservoir portrait. The image data was combined with other datasets, such as petrography of ditch cuttings, pressure, and production data. Other advanced logs were utilized in different modules to characterize the reservoir system behavior. In Fig. 2 the sequence of the workflows is displayed with the input data used in each, to explain how the output of each workflow is integrated into the one that follows.

3.1. Structural framework

Following regional fault trends in the Abu Gharadig Basin, the NEAG 2 structure stands on an upthrown block of the main E-W basin-bounding fault. The major fault comprises two segments, reverse in the east block and normal in the west block. The fault segments are a NE-SW reverse fault and an E-W normal fault, as displayed in steronets C and D in Fig. 3. The southern segment has the NEAG 2-South prospect (SENV, 2008).

3.1.1. Field regional stresses (megascale heterogeneity)

The NEAG 2 development lease consists of two structural compartments: NEAG 2-West (7 wells) and NEAG 2-East (3 wells). Although no structural faulting separates the two segments, each exhibits distinct fault trends (Rashad et al., 2022). In the West block, the structure is defined as a fault-dependent three-way-dip closure with a dimension of 1.7 km. In the East, there are two separate four-way-dip closures with dimensions of 400 and 600 m (Fig. 3). Both

Table 1
A list of NEAG 2 wells from the West to the East with the type of data acquired in each well, the wells with most of the datasets available are labeled as control points.

Data Type	Well Name									
	NEAG 2-3	NEAG 2-1	NEAG 2-2St	NEAG 2-7St	NEAG 2-4St	NEAG 2-6	NEAG 2-5	NEAG 2-E1	NEAG 2-E2	NEAG 2-E3
Drilling Mud	OBM	OBM	OBM	WBM	WBM	WBM	WBM	OBM	WBM	WBM
SGR		*								
GR	*	*	*	*	*	*	*	*	*	*
RES	*	*	*	*	*	*	*	*	*	*
NEU	*	*	*	*	*	*	*	*	*	*
DEN	*	*	*	*	*	*	*	*	*	*
PEF	*	*	*	*	*	*	*	*	*	*
CALI	*	*	*	*	*	*	*	*	*	*
DTC		*								
DTS										
Cement log		*	*	*	*	*	*	*	*	*
TDT			*	*	*	*	*	*		
Fm. Pressure		*	*	*	*	*	*	*	*	*
Fluid Sample		*								
Check-shot		*	*		*		*	*		
Image					*		*	*		
Core										
Ditch cuttings		*			*	*		*		
		Control Point 1			Control Point 2		Control Point 3	Control Point 4		

Methodology
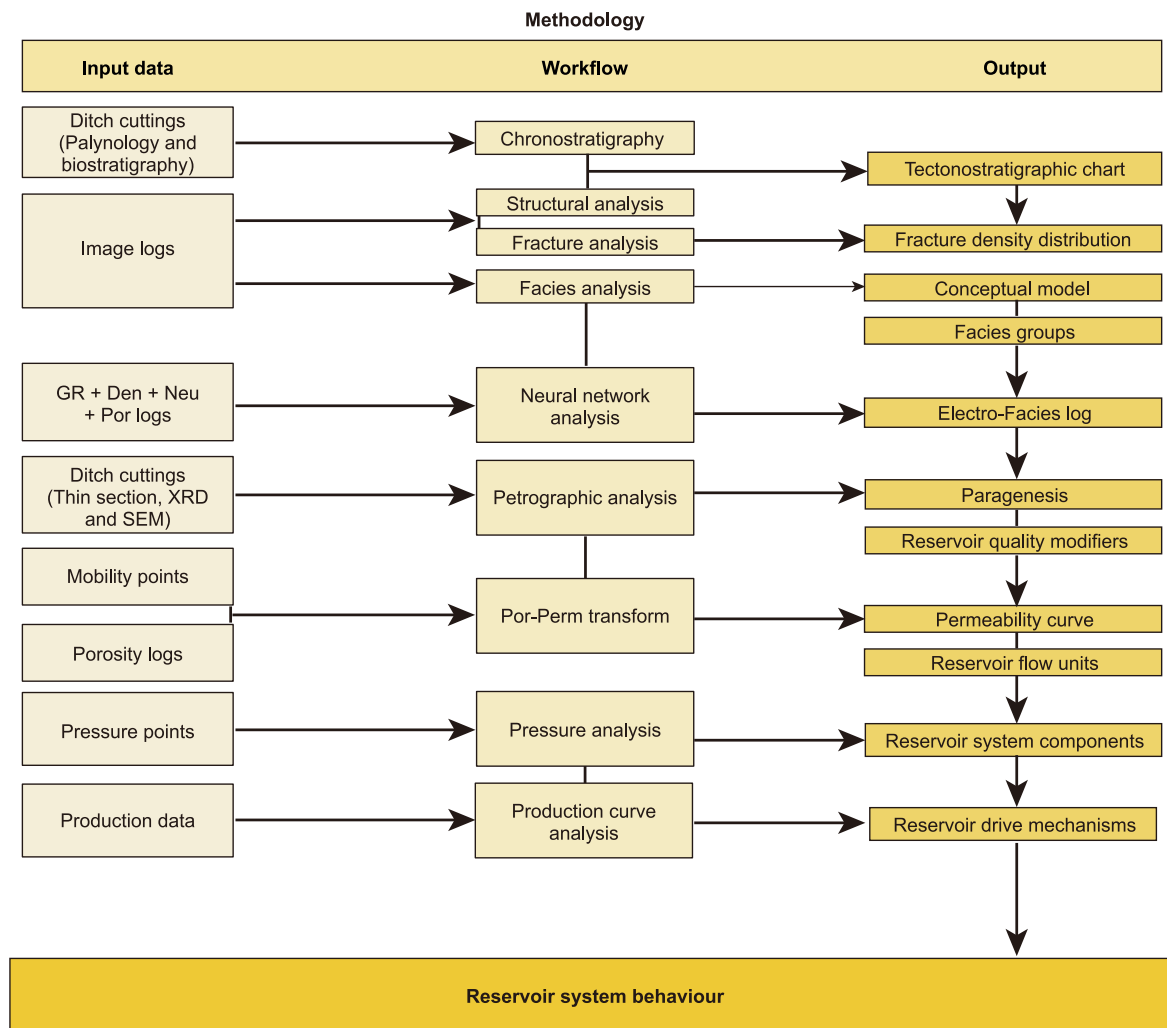
Fig. 2. The workflow matrix of the multiscale reservoir characterisation is described in terms of the input data used in each workflow and their output.

the 3-way dip closure in the west and the four-way dip closures in the East were created due to compression movements during the

Coniacian/Santonian Phase. NEAG 2 bounding fault is believed to be Upper Cretaceous in age, as indicated by the change in the thickness
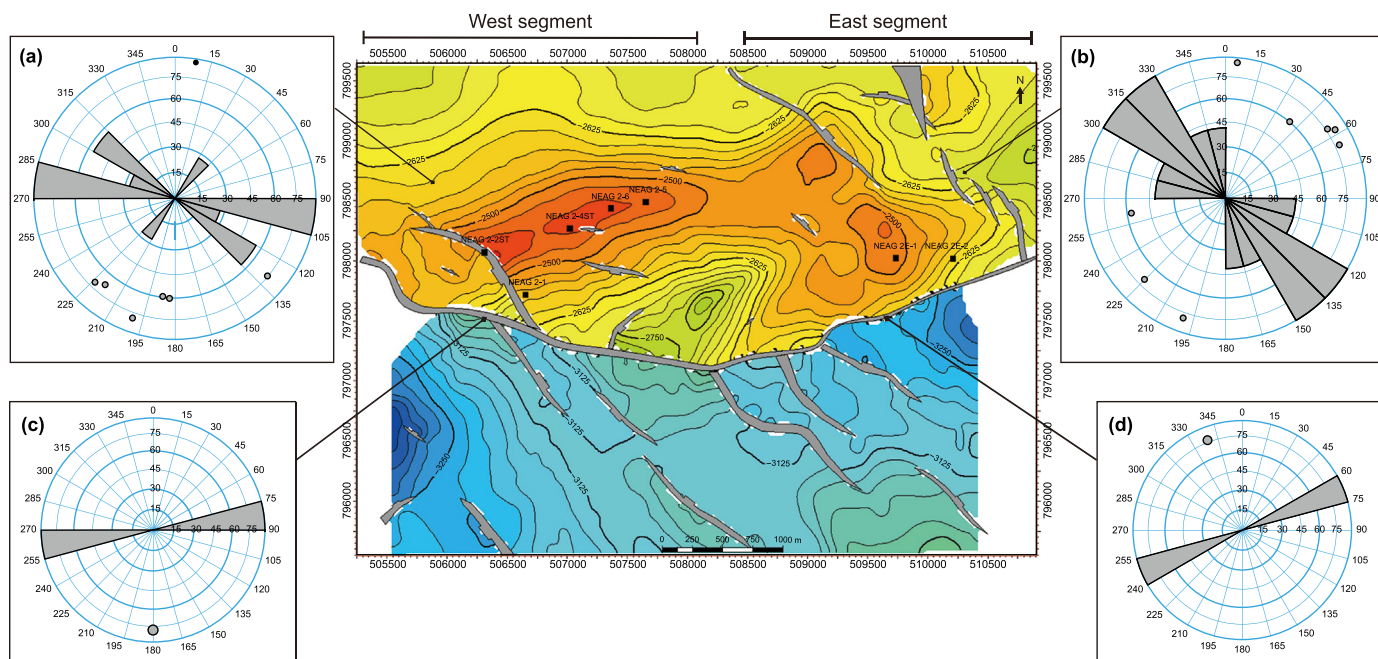
Fig. 3. NEAG 2 Field main reservoir map, with the faults in the West and East Segments, and their strike trends, dip angle, and dip directions plotted on rose diagrams ((**a**) and (**b**)). While (**c**) and (**d**) display the rose diagrams of normal and reverse segments of the major fault, respectively. The map at the bottom shows NEAG 2 Field location in Abu Gharadig Basin (Exported from Petrel, 2017).

of the Khoman Formation (SENV, 2008). The main reverse fault brought the whole structure up with a 600 m average throw.

A stereonet projection was created for faults in each segment (Fig. 3). Each seismic fault is displayed with its strike fan, dip angle, and dip azimuth (black dots). Fisher's statistical model was applied to average the fault trends; the largest fan size reflects the dominant trend. The dominant fault trend in the West segment (Stereonet A) is E-W to NW-SE with subordinate NE-SW directions. While in the East segment (Stereonet B), the NW-SE to N-S trends, with subordinate E-W trends.

3.1.2. Fracture analysis (macroscale heterogeneity)

Describing and counting the reservoir's fractures is critical, as they may significantly affect fluid migration, flow, and accumulation (Mattioni et al., 2010). In terms of field production behavior, such as; early water breakthrough, compartmentalization, and dual permeability, fracture distribution, type, and orientation can be directly relevant to these phenomena in reservoir performances (Nelson, 1985). From the image log structure interpretation conducted by Halliburton (2011, 2015), and Schlumberger (2015a), the results came with different fracture distribution intensities in each well. In NEAG 2-4St well, 51 natural fractures were observed in the processed imaged intervals (Halliburton, 2015). They comprise; 13 semi-conductive fractures, four conductive fractures, 34 resistive fractures, and ten minor faults have been identified in the studied imaged intervals. (Fig. 4). In NEAG 2-5 well, 39 natural fractures were observed in the processed imaged intervals (Schlumberger, 2015a). They include; 35 resistive fractures and 4 conductive fractures. The structural dip analysis showed that the borehole intersected a faulted anticline. It encountered a one-fold limb and went through another minor fault in Kharita Fm. In addition, two possible faults were located at the depths of 2840 and 2773 mD in the Bahariya and Kharita formations. Unlike the other two wells NEAG 2E-1 well, is an oil-based mud, that encountered 129 fractures along the OMRI imaged interval (Halliburton, 2011). The fractures looked resistive, as it is difficult to differentiate the

fracture type in the case of oil-based mud. Three minor faults were recognised, and two possible faults throughout Lower Bahriya and Kharita zones.

Unlike the other two wells NEAG 2E-1 well, is an oil-based mud, that encountered 129 fractures along the OMRI imaged interval (Halliburton, 2011). The fractures looked resistive, as it is difficult to differentiate the fracture type in the case of oil-based mud. Three minor faults were recognised, and two possible faults throughout Lower Bahriya and Kharita zones.

Relative to the field regional stresses, the above-counted minor faults and fractures were projected on a Stereonet window. Two rose diagrams were created, one for the west wells (NEAG 2-4St and NEAG2-5) and one for the East well (NEAG 2E-1) (Fig. 4). In the west segment, the dominant direction of the fractures and faults are in the WNW-ESE with subordinate NW-SE, and WSW-ENE strike directions. Some fractures are dipping in an anti-thetic direction, while others are dipping in a synthetic direction following the regional stresses. On the other hand, the East segment showed a more radiant pattern, considering that it is represented by only one well, which decreased confidence. However, it displayed 2 dominant structural trends in the NNW-SSE and NW-SE directions, corresponding with the regional structural trend.

3.2. Stratigraphic framework

The reservoir section is defined from the Cenomanian Bahariya Formation at the top to the Albian Kharita Formation at the bottom. This interval represents the Early Cretaceous sub-sequence included in the Abu Gharadig Basin Syn-Rift Mega-Sequence (El Gazzar et al., 2016 and references therein). The well log correlation (Fig. 5) revealed that the Lower part of Bahariya and the upper part of Kharita are the hydrocarbon-saturated reservoir section. The Lower Bahariya section is subdivided into 4 main zones; L. Bah-4, L. Bah.3, L. Bah-2, and L. Bah-1, from the basal boundary of Intra Bahariya Limestone (IBL) at the top to Kharita Formation at the bottom (Fig. 5). The upper zone of Lower Bahariya (L. Bah-4)
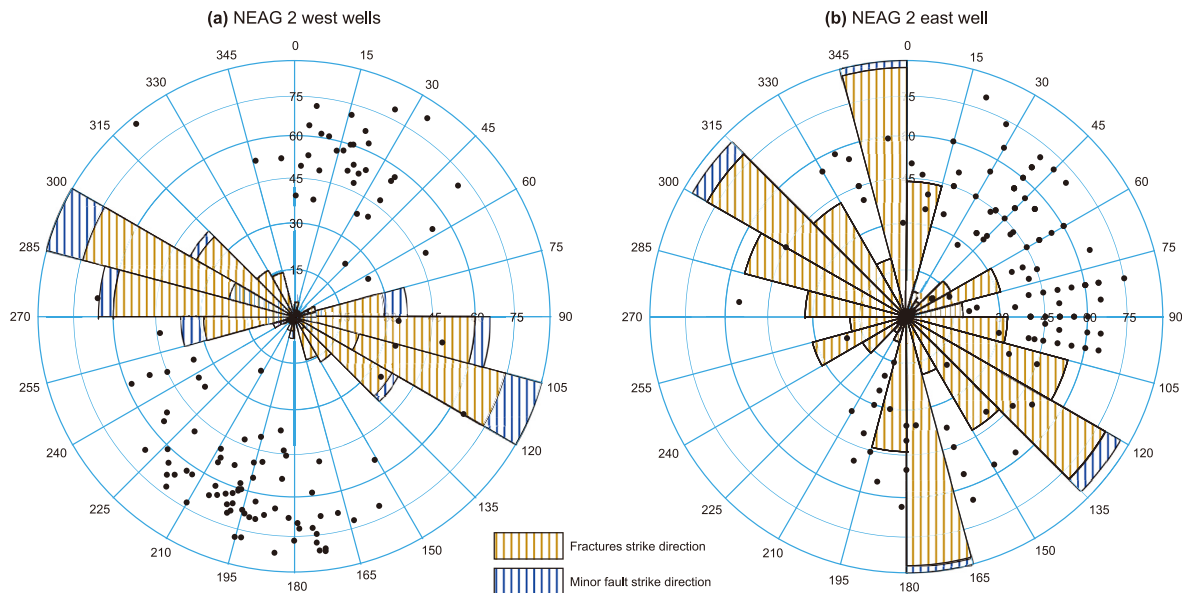
Fig. 4. Stereonet windows display the rose diagrams of the sub-seismic faults (minor faults) and fractures, with their strike trends, dip angle, and dip directions plotted, **(a)** for NEAG 2 west wells and **(b)** for the east well (Exported from Petrel 2017).
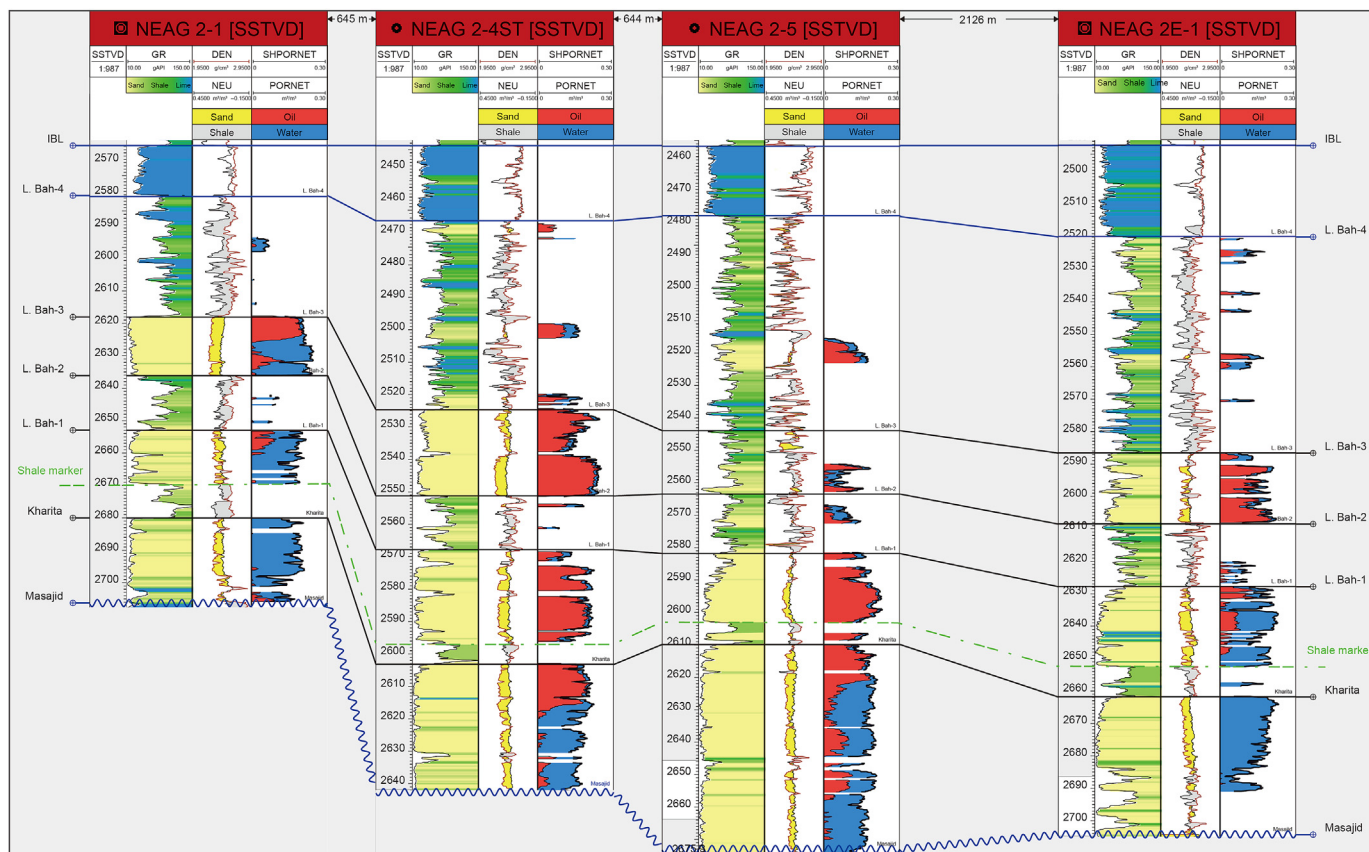
Fig. 5. Well log correlation panel between the 4 wells; NEAG 2-1, NEAG 2-4St, NEAG 2-5, and NEAG 2E-1. It shows the reservoir section zonation and log response, previewing the reservoir character variation vertically and laterally in the wells. The panel is flattened on the IBL marker as the top datum to remove the structure elevations, and the well spacings are also represented (Exported from Petrel, 2017).

underlies the IBL bed, which is the caprock of the system. It was noticed that the bottom of Lower Bahariya is differentiated from the top of Kharita by a shale bed of an average 10 m thickness. This shale marker could be the sequence boundary between the Albian and the Cenomanian Epochs, represented as a green dashed line in Fig. 5. The Kharita section is incomplete due to a period of non-

deposition or erosion, which brought up the Masajid Formation to be directly below Kharita unconformably. The disconformity surface between the Masajid and Kharita bottom is represented by a blue zigzag line in Fig. 5. The top of the Masajid was not penetrated in all wells; thus, it was placed after a specific thickness of Kharita, to create a unified base for the model.

3.2.1. Chronostratigraphy (megascale heterogeneity)

It has been challenging in NEAG 2 to clearly distinguish the top of the Kharita Formation from the base of the Bahariya Formation due to the similarity in reservoir quality between both or the undiagnostic fossil content. Therefore, Biostratigraphic analysis was conducted on two wells, NEAG 2-1 and NEAG 2-4St, for chronostratigraphy and paleoenvironment by SENV (2009) and EREX (2015), respectively. The findings came as the following:

Bahariya Formation of Early Cenomanian, the top of the reservoir section was defined based on the highest occurrence of *Afropollis jardinus* and *Elaterosporites klaszii* palynological zones (Cretaceous C13c/?C13b) from both wells (SENV, 2009; EREX, 2015).

Bahariya-Kharita Formations boundary of Early Cenomanian-? Late Albian time interval couldn't be well-defined from NEAG 2–1 based on; the miospore-dominated assemblages, included *Afropollis jardinus* (rare), *Araucariacites australis* (common), *Classopollis brasiliensis* (rare), *Classopollis torosus* (rare), *Cretacaeiporites cf. scabratus*, *Cyathidites australis/minor* (rare), *Elaterosporites klaszii*, *Ephedripites* spp. (rare) and *Perotriletes pannuceus* (rare), which is typical of the Early Cenomanian/Late Albian palynological zones (Cretaceous C13a/?C12) (SENV, 2009). While from NEAG 2-4St well there was no deeper penetration to define the boundary. The most recent findings on this boundary were found by Hassan et al. (2023), they concluded that the boundary that separates the Kharita Fm from the Bahariya Fm is considered a sequence boundary as it is associated with erosion. The same boundary was studied by Said et al. (2021) in the Abu Sannan Area in the main Abu Gharadig Basin. They defined the Late Albian by *Trilobosporites laevigatus-Stellatopollis* sp. and *Stellatopollis spp. -Convavissimisporites punctatus*. While the Early-Middle Albian was defined by the *Convavissimisporites punctatus-Murospora florida* (Said et al., 2021) which were not found in NEAG 2 wells. This can prove that the complete Albian section in NEAG Area was not deposited or extensively eroded due to later uplifting. The Kharita Formation was found to be unconformably overlain by the Cenomanian Bahariya Formation in some of the nearby basins, such as the Beni Suef Basin. The unconformable stratigraphic relation was detected by a sharp facies change from the gravelly sandstone of the fluvial Upper Kharita Formation to the shallow marine facies of the overlying Bahariya Formation (Shehata et al., 2018).

Masajid Formation of Late/Middle Jurassic (Oxfordian/Callovian) age was defined by the highest occurrence of *Korystocysta gochtii* and *Gonyaulacysta jurassica* palynological zone (Jurassic J7a-J5) from NEAG 2-1 well, together with the subsequent high occurrence of agglutinated foraminifera and *Nautiloculina*? sp. and the rare occurrence of *Ammobaculites*? sp. (SENV, 2009).

3.3. Facies analysis (Mesoscale heterogeneity)

The reservoir facies heterogeneity was analyzed on the mesoscopic scale using BHI interpretation in NEAG 2-5, NEAG 2-4ST1, and NEAG 2E-1 wells. Then the resulting facies characterisation was extrapolated in the uncontrolled areas. The micro-resistivity variations are translated to lithofacies characteristics such as bedding sequences, sedimentary structures, and vertical grain-size successions by creating a set of diagnostic criteria (Javier et al., 2010). Sedimentary dip data with image interpretation provided a well-

developed understanding of the depositional processes, reservoir geometry, and paleocurrent indicators. Schlumberger Team conducted a sedimentological study in 2015, of which the main output was the correlation of the depositional facies of the Lower Bahariya-Kharita reservoir sequence. The following analysis is guided by the results reported in Schlumberger (2015).

3.3.1. Lower Bahariya-Kharita facies associations

The depositional facies interpretation was presented for the main stratigraphic units of the Kharita-Lower Bahariya Reservoir System; the Lower Bahariya zones are abbreviated to L. Bah as, L. Bah-4, L. Bah-3, L. Bah-2, and L. Bah-1, topped with Intra Bahraiya Limestone (IBL) marker and bottomed by Kharita. The main features of the reservoir facies interpretation were described per zone. Each reservoir zone was defined by its depositional setting, depositional elements, the facies associations, and their evidence.

3.3.1.1. Kharita Zone.
Depositional setting: coastal fluvial plain with tidal influence. Depositional elements: tidally influenced channel belt, stacked distributary channels, and bay-fill deposits. Lithofacies: bedded sand, cross-bedded sand, sand with mud clasts, laminated sand, shaley sand, massive sand, and massive shale (Fig. 6).

Evidence and discussion: Channel-belt deposits were evidenced by fine to medium-grained kaolinitic erosional-based sandstones with reactivation surfaces (Schlumberger, 2015b). In addition to dispersed intra-formational mud clasts and extra-formational reworked pebbles at the base, with a blocky to faint fining-upward pattern. The thick stacked sand bodies, laterally continuous, point to constant fluvial input. The tidal influence was demonstrated by discontinuous/continuous mud drapes, bipolar paleo currents, reactivation surfaces, and the dominance of mud clasts along fore-sets and bedding planes. The associated tidal criteria reflect their deposition on a coastal plain, where tidal currents had reworked the sandstones. This tidal influence is recorded at these channels' lower reaches and seaward terminations and suggests that they were deposited on the coastal plain fluvial-tidal transitional setting. A typical fluvial origin as a single source for the deposition of the Kharita Formation was excluded due to; the relative fine-grained size of sandstones, absence of fine floodplain roots or paleo-exposure criteria, absence of intensive scoured surface, and lack of high variability in paleo-current azimuth which commonly prevails in the fluvial setting. The stacked channels commonly elucidate vertical superimposed stories, where upper stories are usually incised into lower stories, suggesting channel reoccupation during migration or avulsion (Li and Bhattacharya, 2014). The most abundant sedimentary features are trough and planar cross-bedding and parallel lamination. Pebbles and mud clasts were found dispersed along channel thalweg.

3.3.1.2. L. Bah-1 zone.
Depositional setting: estuarine embayment. Depositional elements: stacked tidal channel sandstone, tidal bar sandstone, mixed tidal flat shaley sandstone, and estuarine mudstone (Fig. 6). Lithofacies: Bedded sand, cross-bedded sand, flaser-bedded sand, heteroliths, deformed sand, laminated sand, shaley sand, estuarine mudstone, massive sand, and massive shale.

Evidence and discussion: tidal channels with fining-upward depositional motifs, cross-bedded, and laminated glauconitic sandstone were recorded in this zone. Since the glauconitic facies are characteristic of the open-marine environment, which is moderately alkaline (Odin and Matter, 1981), this zone remarks the marine influence with the beginning of sea level rise. Mud drapes and reactivation surfaces pointed to the deposition in a subtidal setting in a tidal-dominated estuary (Schlumberger, 2015b). Tidal channels displayed lower dimensions (width and thickness)
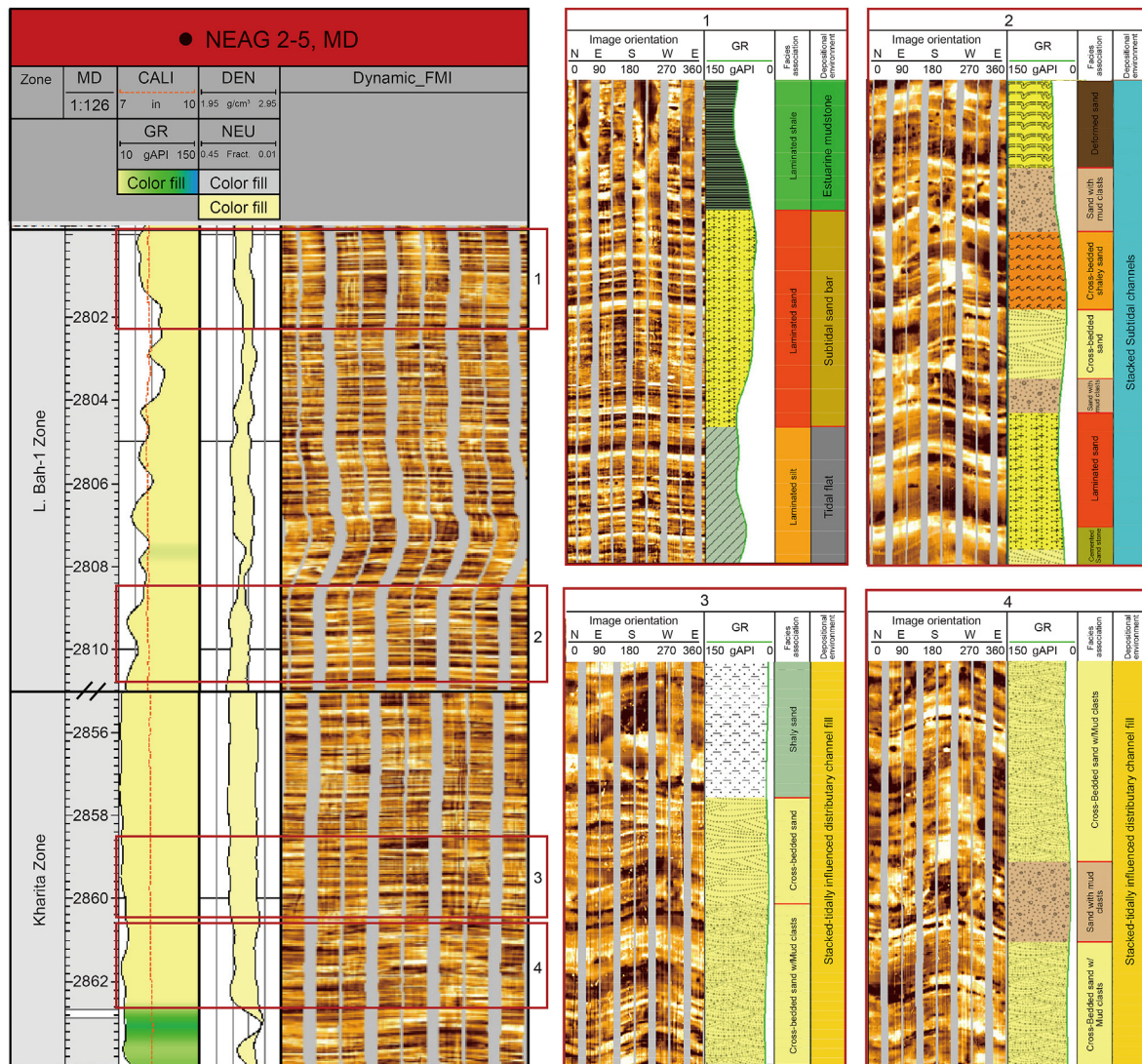
Fig. 6. An example of image log facies interpretation from NEAG 2−5 well, 4 intervals are enlarged to show the detailed facies response on the image log. The four intervals display the facies variation from Kharita Zone at the bottom (Intervals 3 and 4) to L. Bah-1 Zone at the top (Intervals 1 and 2) (Modified after Schlumberger (2015b).

relative to the fluvial channels of the coastal plain recorded in Kharita Formation. However, the apparent thickness of these tidal channels in the L. Bah-1 Zone is larger than in the shallower zones. This high thickness reflected that most sandstones were sourced from the underlying fluvial sandstones of the Kharita Formation. These sediments were reworked by tidal currents during the marine transgressive event at this zone and represent the early filling of the large estuarine embayment at the base of the Bahariya Formation.

3.3.1.3. L. Bah-2 zone. Depositional setting: estuarine embayment. Depositional elements: mixed tidal flat and estuarine mudstone facies with tidal bar sandstone. Lithofacies: laminated shale, bioturbated sand, calcareous shale, carbonates, massive siltstone, sand with mud clasts, laminated siltstone, shaley sand, bedded and massive shale, estuarine mudstone, rippled sandstone, shallow marine carbonates.

Evidence and discussion: the dominance of fine-grained facies indicates a significant decrease in current strength as reflected in the thin thicknesses of sandstone beds compared to the underlying L. Bah-1. This zone demonstrated an increase of the intertidal flat

with mixed mudstone and sandstone laminae. The estuarine mudstones are the typical facies in this zone, comprising laminated siltstone and massive, bedded shale.

3.3.1.4. L. Bah-3 zone. Depositional setting: estuarine embayment to shoreface. Depositional elements: tidal channels, subtidal sand bar sandstone, mixed tidal flats transgressive sandstone (shoreface deposits), and shelf shale. Lithofacies: cross-bedded, flaser-bedded sand, shaley sand, bedded sand, laminated sand, laminated silt, cemented sand, bioturbated silt, sand with mud clasts.

Evidence and discussion: this reservoir zone elucidated variability in lithofacies among the wells. For example, the subtidal sand bars and tidal channels in NEAG 2-4St, which are 25−27 m thick, were changed into shelfal shale with some streaks of sand in NEAG 2-5 well. Since both wells are 644 m apart, this facies variation suggested that both channels and bars are of smaller dimensions. While in NEAG C5 E-1 well, the sandstone facies reflected the deposition in tidal channels and subtidal sand bars but with a lower quality than those in NEAG 2-4St. This quality variation proved that the sand in NEAG 2-4St is not connected at the level of the L. Bah-3 Zone, unlike the widely extended sand of the L.

Bah-1 Zone. The tidal flat depositional suite was evidenced by the presence of flaser and wavy bedded sandstones and heteroliths. Transgressive sandstone represents the shoreface facies deposited during flooding events or storm conditions. The deposits of this zone reflect a steady increase in the marine processes associated with the rise of sea level.

3.3.1.5. L. Bah-4. Depositional setting: shallow marine. Depositional elements: transgressive sandstone, tidal sand bar sandstone, and mudflat. Lithofacies: laminated sandstones and carbonate beds.

Evidence and discussion: this zone is characterized by the prevalence of shelfal shale and an upward increase in the frequency and thickness of carbonate beds (Fig. 5). In addition, transgressive sandstone and tidal sand bars are chiefly built of laminated sandstones and shaley sand. This zone demonstrated a rapid rise in sea level and low energy conditions to allow the deposition from the suspension of shales (Schlumberger, 2015b). Carbonate facies are linked to a relative decrease in sand supply. The transgressive sandstones reflect deposition in a lower shoreface, where mud laminae are attributed to deposition or bioturbation during quiescent episodes. The sediments of this zone represent the topmost part of the filling of the large estuarine embayment and reflect the dominance of the marine processes.

3.3.1.6. IBL zone. Depositional setting: shallow shelf. Depositional elements: shelfal shale and carbonates. Lithofacies: bedded, argillaceous, and nodular limestone, bedded, and calcareous shale.

Evidence and discussion: this sedimentary unit is fairly distinguished in the studied wells and shows regional correlation. This carbonate interval points to a complete cessation of sand supply during a rapid rise in sea level (Schlumberger, 2015b), culminating in the deposition of the Intra-Bahariya Limestone (IBL) bed. IBL is the seismic marker for the field and is encountered in the three wells as a complete section of an average 20 m thickness. This zone represents a prevalence of marine processes after the complete filling of the underlying estuarine embayment.

3.3.2. Neural network analysis

The facies interpretation from the BHI logs should be utilized in the three-dimensional facies model. This would be achievable by using the facies logs as control points and interpolating them in uncontrolled areas. Based on the neural network technology (Kohonen algorithm), it predicts and propagates the rock classification groups. The neural network approach is a computational system that simulates the human brain's biological neural networks (Rogers et al., 1992). The application of neural network technology is beneficial in handling massive amounts of variables (well logs) as an automated method for lithology determination. The learning processes are based on several algorithms, among which backpropagation is the most popular and the standard-used algorithm (Rumelhart et al., 1986).

3.3.2.1. Facies grouping. As mentioned before, the detailed facies analysis produced 23 lithofacies that should be grouped into distinctive associations for static modeling. As in the workflow by Samantray et al. (2010), the facies grouping was according to lithology and reservoir quality, not the depositional setting. In addition, in the reservoir rock typing done by Mehrabi et al. (2019), the petrographic characters were integrated with petrophysical logs and por-perm measurements for the reservoir quality evaluation. Based on this, the depositional facies were grouped into three categories (rock types), depending on their reservoir quality.

In our workflow, we categorized the reservoir depositional facies into four groups (rock types) based on their sedimentary structures and depositional processes. Referring to the laws of hydrodynamics that control sediment transportation and deposition, the lithofacies were grouped into four types. Considering the main variables are the flow velocity versus the grain diameter, shape, and density, some criteria were stated. A facies of fine grain size (<0.004 mm) would dictate low flow velocity, where clay size is transported more easily than sand-grade material (Nichols, 2009). On the other hand, high current velocity or strength is indicated by the deposition of coarse-grained facies, i.e., sand to pebbles up to (10 mm) in size. In sand facies, the sedimentary structure is usually a supporting current strength indicator. Although each sedimentary structure results from a specific depositional process, it cannot be exclusive to a single environmental setting. This distinction is important because, within a single depositional setting or subenvironment, different lithologies with varying reservoir properties may coexist (Samantray et al., 2010). Accordingly, cross-bedded sand would reflect a stronger current ($0.4–2$ ms^{-1}) than laminated or flaser-bedded sand ($0.6–2$ ms^{-1}). Scour-based sand or pebbly sand would correspond to the highest current strength (<2 ms^{-1}) (Martín-Chivelet et al., 2008). The current strength will be directly proportional to the facies quality in grain size, sorting, and shale content.

As a result, four facies groups were assigned to the interpreted lithofacies and corresponded to different qualities (Fig. 7): **Facies Group 1:** the current velocity is very high, transporting the coarser grains in the system and creating crossbedding or scoured base (Fig. 7). This facies type could be embodied as Tidal Channels since an erosive surface marks tidal channels with mud intraclasts and load casts (Al-Moqaddam et al., 2018). They were supported by the dominancy of the cross-bedded and pebbly sandstones. **Facies Group 2:** the current velocity is moderate to high (alternative current), transporting the coarse sand but with some indication of low current strength, creating flaser-bedded, cemented, or massive sandstone. This facies type could be embodied as Tidal Sand Bars (Fig. 7). According to Martín-Chivelet et al. (2008), flaser bedding, where the muddy sediment is subordinate, indicates settling fine-grained sediment from suspension during short periods of weak currents. **Facies Group 3:** the current velocity is low, transporting the fine-grained sand and silt. It created laminated or bioturbated shaley sandstone. This facies type could be embodied as Mixed Tidal Flats, which might be confused with the tidal sand flat. However, mixed flats are silty to muddy sandstone interbedded with sand (Al-Moqaddam et al., 2018). As in NEAG 2-5 well, heteroliths are the dominant lithofacies that would represent mixed tidal flats. Therefore, it would be better to consider it as Mixed Tidal Flats to represent the lowest facies quality (Fig. 7). **Facies Group 4:** the current velocity is very low or quiescent, transporting shale and clay, precipitation of lime and mud, and marine fauna, they are grouped as the background non-reservoir facies. Each facies group was given a code; the facies group codes were exported for each well in a discrete log named (**Facies code**). This log was then used in the IPSOM module as the classification group indexation data set.

3.3.2.2. IPSOM workflow. Using Techlog 2015 Software, IPSOM module workflow was applied. This module applies the neural network algorithms to predict the facies in those wells with no facies interpretation either from core or image data. The wells with facies description were used as control points, from which the facies indexation was learned.

3.3.2.2.1. Input data selection. This step aimed to select a representative data set to be involved in the modeling operation. In this case, the best representative for the facies type was GR, DEN/NEU, and Pornet logs. Each variable (log type) was given a weight

NEAG 2-4St

Group		Thickness
1	Cross-bedded sand	29.5
	Cross-bedded sand w/mud clasts	16.3
	Cross-bedded sand w/intraclast	10.0
	Sand with mud clasts	8.7
	Bedded sand	3.5
	Total	68.0
2	Laminated sand	14.9
	Flaser bedded sand	5.8
	Cross-bedded calcareous sand	3.1
	Massive sand	0.9
	Cemented sand	0.2
	Total	25.0
3	Shaly sand	18.2
	Sandy shale	12.0
	Calcareous sand	0.9
	Total	31.1
4	Massive shale	13.6
	Bedded shale	8.5
	Carbonates	6.8
	Shaly carbonate	2.8
	Marl	2.0
	Laminated shale	1.6
	Calcareous shale	0.8
	Nodular Carbonate	0.5
	Total	124.1

NEAG 2-5

Group		Thickness
1	Cross-bedded sand	36.9
	Cross-bedded sand w/mud clasts	16.9
	Bedded sand	8.2
	Sand with mud clasts	5.2
	Cross-bedded pebbly sand	1.4
	Pebbly sand	0.7
	Total	69.3
2	Laminated sand	10.4
	Massive sand	3.7
	Deformed sand	3.7
	Cemented sand	2.2
	Flaser bedded sand	1.1
	Total	21.0
3	Laminated silt	9.9
	Shaly sand	9.8
	Bioturbated siltSt	1.3
	Flaser bedded shaly sand	0.8
	Heterolithics	3.465218
	Total	25.3
4	Bedded shale	24.3
	Laminated shale	16.2
	Calcareous shale	13.2
	Massive shale	6.7
	Nodular carbonates	3.4
	Total	63.8

NEAG 2E-1

Group		Thickness
1	Cross-bedded sand	33.3
	Bedded sand	15.2
	Total	48.5
2	Laminated sand	14.8
	Massive sand	11.4
	Total	26.4
3	Laminated silt	12.8
	Shaly sand	5.8
	Massive siltstone	1.2
	Total	19.8
4	Massiveshale	60.5
	Laminated shale	19.2
	Bedded carbonate	17.9
	Bedded shale	16.6
	Calcareous shale	16.1
	Carbonate	16.0
	Total	146

Type 1	High current strength
	Tidal channels

Type 2	Moderate current strength
	Tidal sand bars

Type 3	Low current strength
	Mixed tidal flats

Type 4	No current
	Tidal mud flat

Fig. 7. The list of lithofacies grouped into 4 main types, guided by the sedimentary structures and their current velocity implications, with their corresponding facies body geometries.

value to assign each variable as a high or low-weighted component. Since this dataset was used as an input to be correlated to the facies code, the three wells with Facies code logs were the control points for the (Learn/Index) process. While the offset wells with no Facies code logs were set for the (Apply to) process (Fig. 8a).

3.3.2.2.2. Indexation. In this process, the nodes with similar petrophysical properties were regrouped to be assigned to one of the facies groups. Thus, the Facies code log was used as the indexation input. After selecting the indexation input, the classification method was set as a supervised method. Once the model had learned the link between petrophysical properties and facies, the IPSOM module was applied. Then it created a classification facies curve for the other wells. The indexation group the points with similar behavior on the Kohonen map, as it is a supervised mode. Since the facies code log was used as the indexation input, it calibrated the map and found a relation between the inputs variables (logs) and the output (facies classification curve).

3.3.2.2.3. Neural analysis. After all the parameters had been adequately defined, IPSOM started the learning and indexing phases. A self-organizing map (SOM) structure was created based on a 2D or 3D Sammon Projection (Fig. 8b). In the Sammon map projection, the deployment of the distance between each node on the map was visually checked. The resulting self-organized map's size is defined by its number of nodes. The created map has a 20*20 dimension (400 nodes), and each unit appears as a rose diagram composed of the input logs (GR, DEN/NEU, and Pornet) (Fig. 8c). Each neural unit was excited by one specific well log response combination. Each node used the four input logs to reflect a particular spectral composition displayed as a rose diagram. The highest probability defines the label of the node, from which each facies type was quantitatively classified (Fig. 8c). Finally, the 2D indexed self-organizing map demonstrated the geological interpretation of log data and facies prediction.

3.3.2.2.4. Model refinement and quality control. The output map could have been edited manually in the areas of misleading data by qualitatively comparing the input and output logs. Otherwise, from the statistical information for each class or facies group. In the (output statistics tab), the mean and variance of each input variable within each facies group were tabulated (Fig. 8d). For example, GR values range from 20 API in Facies Type 1 to 71API in Facies Type 4, reflecting the cleanest sand facies to shale facies, respectively.

3.4. Petrographic analysis (Microscale heterogeneity)

Petrographic analysis was conducted on ditch cuttings of NEAG 2-4St, NEAG 2-6, and NEAG 2E-1 as compensation for the gap in whole-rock core data. The petrography of the detrital and authigenic components was identified and characterized by different textural and mineralogical compositions (Corex, 2019). The petrographic analysis, including thin section, SEM, and XRD, provided insight into the microscopic reservoir facies heterogeneity. For the micro-scale characterization, different micro-facies types were described and quantified.

3.4.1. Microfacies types

The relative abundances of major detrital and authigenic components were described per zone, as Corex (2019) reported. Quartz Arenites, Quartz Wackes, Sub-feldspathic Arenites, and Sub-feldspathic Wackes are the main 4 micro-facies types. They occur in various proportions in different zones. Most of the sample's accessory minerals (Glauconite, Kaolinite, Chlorite, Siderite) exceed 20% of the rock composition. These accessory minerals gave a variety of the main 4 micro-facies such as Glauconitic/Kaolinitic/Chloritic/Sideritic Quartz and Subfeldspathic Arenites, or Glauconitic/Kaolinitic/Chloritic/Sideritic Quartz and Subfeldspathic Wackes (Fig. 9). The relative proportion and distribution of each microfacies in the reservoir zones are listed in Table 2.

3.4.2. Diagenetic history

The integrated petrographic analysis (thin section, SEM, and XRD) revealed that the sedimentary succession was affected by several diagenetic processes that influenced the reservoir system quality in return. Estimating the original composition and subsequent diagenetic quality modifiers is essential for sandstone reservoir quality prediction (Hartmann and Beaumont, 1999). Diagenetic processes are described in three stages: Eo-diagenesis, Meso-diagenesis, and Telo-diagenesis.

A succession of diagenetic events with increasing depth was established to identify the diagenetic sequence for Lower Bahariya-Kharita Reservoir. This sequence was guided by the primary components available and the secondary diagenetic products that occur in a known sequence. The relation between the mechanical and chemical diagenetic processes that occurred in the reservoir

IPSOM workflow

(a)

Well	Dataset	Gamma ray	Porosity	Bulk density	Neutron porosity	Classification group	Data set type
NEAG 2E-1	LQC	GR	PORNET	DEN	NEU	Facies code	Learn/index
NEAG 2-4ST	LQC	GR	PORNET	DEN	NEU	Facies code	Learn/index
NEAG 2-5	LQC	GR	PORNET	DEN	NEU	Facies code	Learn/index
NEAG 2-1	LQC	GR	PORNET	DEN	NEU		Appyly to
NEAG 2-6	LQC	GR	PORNET	DEN	NEU		Appyly to
NEAG 2E-2ST	LQC	GR	PORNET	DEN	NEU		Appyly to
NEAG 2-2	LQC	GR	PORNET	DEN	NEU		Appyly to

(c)

(b)

(d)
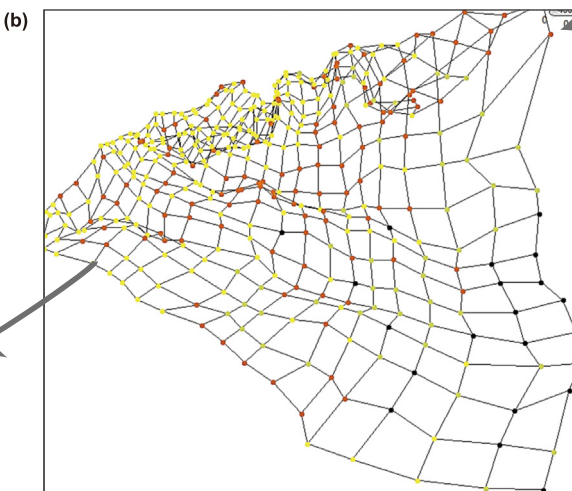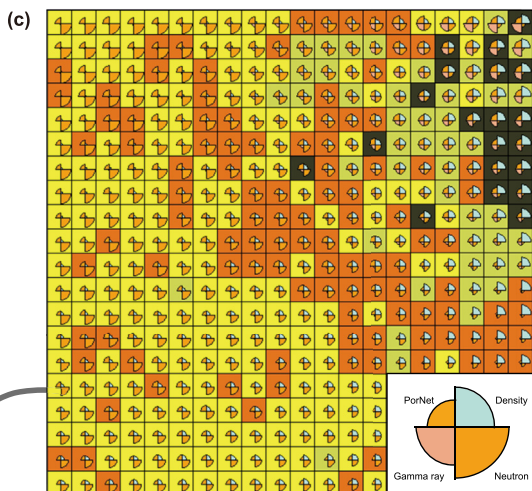
	Facies type 1		Facies type 2	
Color				
Number of samples	209		120	
Variables	Mean	Variance	Mean	Variance
Gamma ray	25.0180	212.7772	31.5292	211.4657
Porosity	0.1639	0.0009	0.1441	0.0013
Bulk density	2.3575	0.0033	2.3935	0.0047
Neutron porosity	0.1405	0.0005	0.1369	0.0011

	Facies type 3		Facies type 4	
Color				
Number of samples	209		120	
Variables	Mean	Variance	Mean	Variance
Gamma ray	50.3809	460.0544	71.4641	283.5650
Porosity	0.1114	0.0009	0.0856	0.0007
Bulk density	2.4513	0.0033	2.4988	0.0025
Neutron porosity	0.1458	0.0009	0.1643	0.0003

Fig. 8. The IPSOM workflow steps. **(a)** The (input data selection) process window. **(b)** The 2D Sammon projection topological map, which is originally composed of n dimensions. **(c)** the self-organized map, 20*20 dimension (400 nodes), Each unit appears as a rose diagram composed of the input logs (GR, DEN/NEU, and Pornet). **(d)** the output statistics table, in which each output (Facies type) has mean and variance values corresponding to each variable (Input logs) (Exported from Techlog, 2015).

sequence was represented in the context of a paragenesis diagram.

3.4.2.1. Paragenesis. Paragenesis is the graphic presentation that describes the relative sequence or timing of "events" in the diagenetic history of a rock, which can include relative age

determinations. Commonly, geologic events do not occur sequentially, as they may overlap temporally. Compaction, dissolution, and cementation processes occur simultaneously in most cases (Ulmer-Scholle et al., 2016). The petrographic analysis was the main lead in creating reservoir paragenesis regarding the reservoir system

Qz: Quartz   Ks: K-Feldspar   Dc: Detrital clays   G: Glaucony   fD: Ferron Dolomite   Sd: Siderite   ✐ : Micro fractures
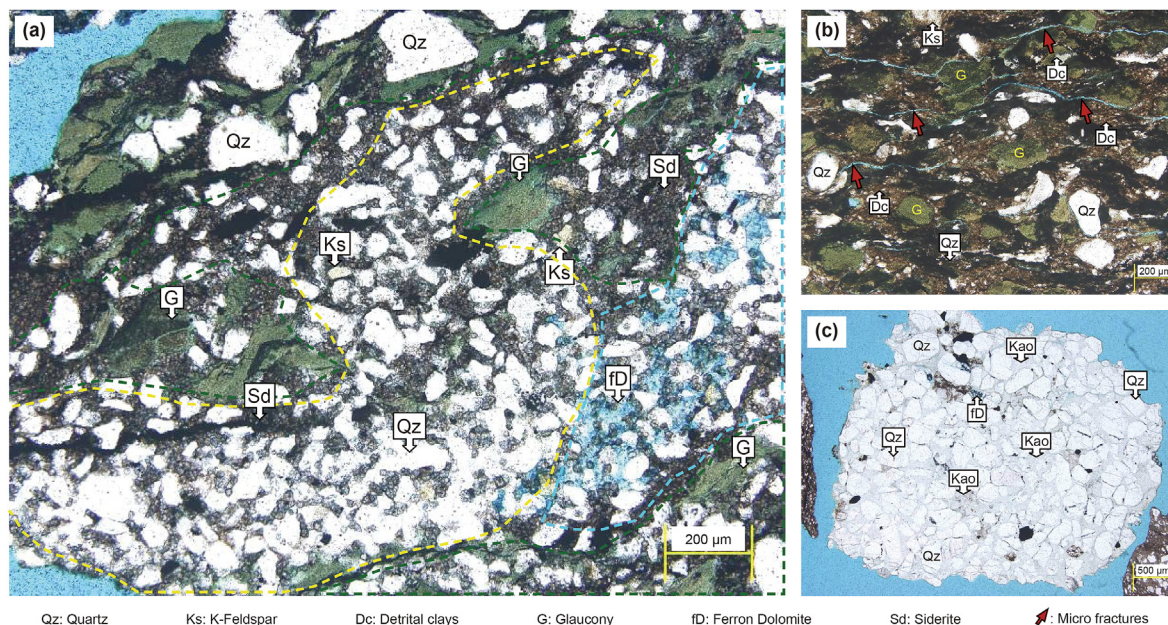
Fig. 9. Selected thin sections from the petrographic analysis depicting the reservoir facies heterogeneity. **(a)** The facies vary on a micrometer scale. **(b)** The glauconitic facies are dominant in the shallow zones, while in **(c)**, the Kaolinitic quartz arenites facies are more dominant in the bottom zones (After Corex (2019)).

Table 2
The distribution and proportions of sand microfacies per zone.

Zone	Dominant Sand Microfacies
L. Bah-4 60m	Glauconitic subfeldspathic arenite
	Subfeldspathic arenite
	Subfeldspathic wacke
	Glauconitic subfeldspathic arenite
L. Bah-3 25m	Sideritic subfeldspathic arenite
	Kaolinitic subfeldspathic arenite
	Glauconitic quartz arenite
	Ferroan dolomitic quartz arenite
	Quartz arenite
L. Bah-2 15m	Subfeldspathic wacke
	Chloritic subfeldspathic arenite
	Glauconitic subfeldspathic arenite
L. Bah-1 25m	Quartz wacke
	Subfeldspathic wacke
	Sideritic quartz arenite
	Glauconitic subfeldspathic arenite
	Kaolinitic quartz arenite
Kharita 65m	Kaolinitic quartz arenite
	Ferron dolomitic quartz arenite
	Kaolinitic sub-feldspathic arenite
	Sub-feldspathic wacke
	Chloritic subfeldspathic arenite

paleo-environment and the regional setting of the area. Since the depositional pore-water chemistry of sandstone is a function of the depositional environment, the Lower Bahariya-Kharita reservoir of the transitional depositional system is expected to include both marine and non-marine influences.

The thin section description gave evidence for geologic processes. A sequence of events in one area of a thin section might not apply to the entire zone, much less to a whole field (Ulmer-Scholle et al., 2016). Therefore, paragenesis was constructed regarding the uncertainty of temporal and spatial variations, flagged when
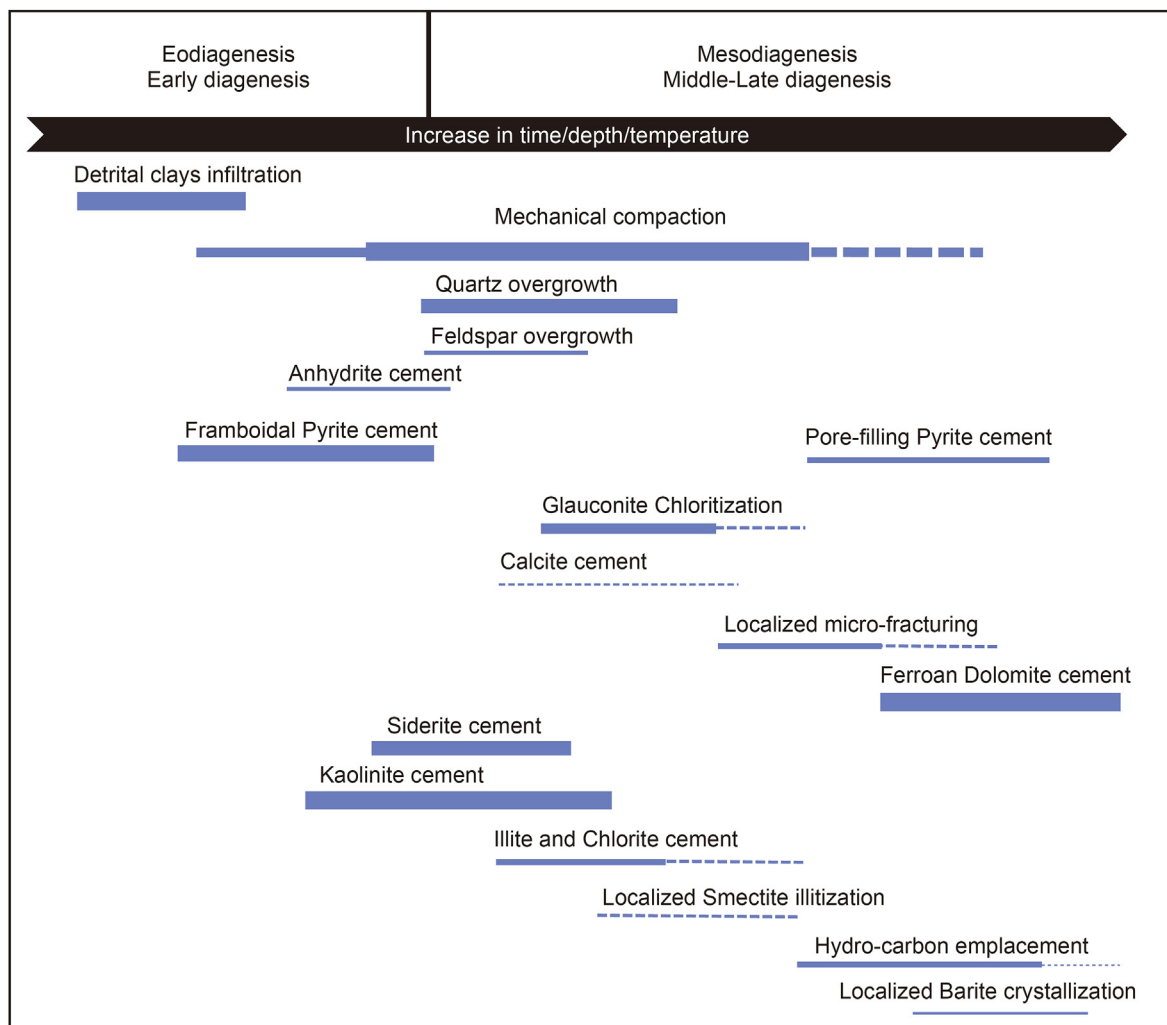
Fig. 10. The Paragenesis diagram illustrates the sequence of diagenetic processes evidenced to occur in the reservoir system.

needed. Paragenetic data are presented in un-scaled bar charts (Fig. 10), portraying the prolonged diagenetic events. These events can overlap and commonly have uncertain starting and ending points. In creating paragenesis for a reservoir system, specific kinds of petrographic observations should be well-thought-out, by which the relative timing is indicated, such as; cement stratigraphy, packing density, and grain deformation (Ulmer-Scholle et al., 2016). Fig. 10 displays the paragenetic sequence for the Bahariya-Kharita reservoir, in which the possible early, intermediate, and late diagenetic processes are outlined as follows.

The freshly deposited unconsolidated sand contains unstable grains that survived weathering, erosion, and transportation at the early diagenetic phase. Before the rock compaction, the pore spaces were prone to be filled with cementing material. The precipitation of clay minerals, silica cement, and feldspars was the first to be incorporated into the reservoir, as Hartmann and Beaumont (1999) defined the typical sequence of cementation. This cementation was followed by quartz crystallization and continued for an extended period. Then carbonates and sulfates were precipitated, as observed in the samples. As reported before, glauconitic facies were abundant in most of the Lower Bahariya zones. The substrate of glauconitization is high alumina smectite, illite, or degraded mica (Odin and Matter, 1981). Calcium sulfate was precipitated as anhydrite pore-filling cementation. The occurrence of anhydrite indicated

that a body of seawater becomes wholly or partially isolated from the open ocean in arid conditions (Nichols, 2009). Excessive pyrite cementation was recorded, which might be formed in two different generations. With the continuous silica precipitation out of the pore fluids, it nucleated on the surfaces of quartz grains and resulted in crystal growth. The euhedral, smooth-faced, and pyramidal quartz overgrowths accompanied minor feldspar overgrowth. Iron carbonate crystallized as siderite, which indicated the mixing of seawater and fresh water under reducing conditions (Nichols, 2009). Calcite cementation was recorded solely in the lime-mudstone or bioclastic limestone facies, but it would have acted as a source of carbonate elements.

Simultaneously with progressing burial, mechanical compaction was initiated, re-oriented the elongated grains parallel to the bedding, developing long-grain contacts and bulk volume reduction. With increasing overburden pressure, dissolution started to occur at grain boundaries, and dissolution of feldspars and glaucony occurred. Then, chlorite started to replace glaucony pellets, building its grain coating rims. The color of the glaucony pellets varies between dark green to light green at the rims and greenish yellow in some other locations (Figs. 9 and 11). This color variation indicates that there are detrital, diagenetic, and chemically weathered glauconite minerals, respectively (El-Sharkawi and Al-Awadi, 1982).
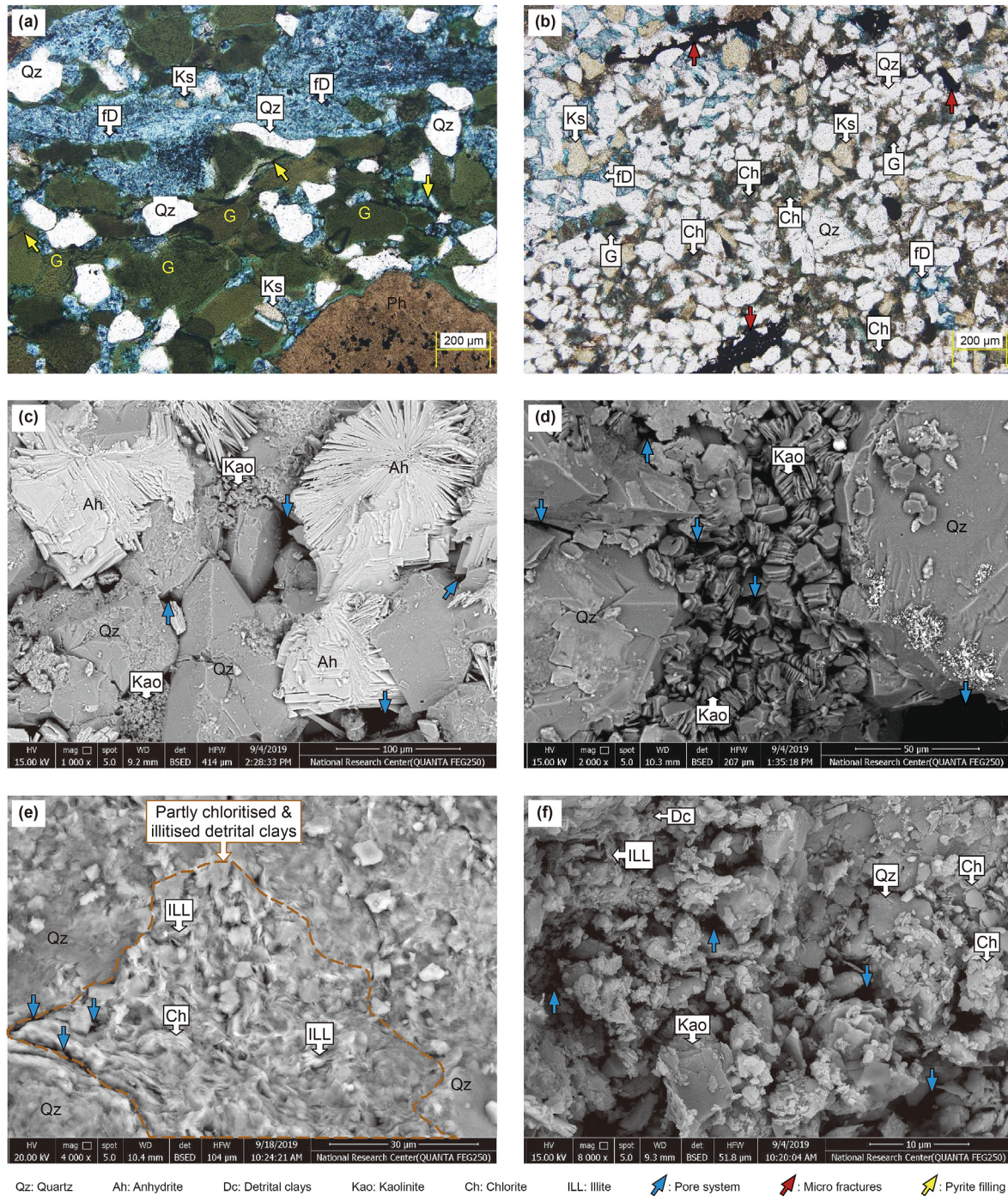
Fig. 11. Selected thin sections to show the relative timing between the diagenetic processes. **(a)** The glauconite grains tend to be compacted and slightly fractured, also invaded by the ferron-dolomite crystals (FD). **(b)** The Ferron-dolomite crystals fill the pore spaces, and the fractures are filled with hydrocarbon. Selected SEM photos from the petrographic analysis display various authigenic components are shown in sections **(c)** well-crystallized anhydrite crystals, **(d)** well-crystallized kaolinite booklets, **(e)** chlorite and illite fibrous behavior, and **(f)** the three clay types coexisted in the same spot (After Corex (2019)).

Micro-fractures were locally recorded in the NEAG 2E-1 well, which affected most of the zones as described in some samples (Fig. 11). The dolomitization process followed this fracturing to form ferroan dolomite cement crystals of small rhomb-shape, as evidenced by cross-cutting relationships depicted in Fig. 11.

Remarking the meso-diagenetic phase, the dissolution, and alteration of earlier, unstable carbonate cement, bioclasts, or lithoclasts began. Such carbonate dissolution, along with the dissolution of calcic feldspars and some clay mineral transformations,

provided the primary source of material for meso-diagenetic carbonate cement (Ulmer-Scholle et al., 2016). Kaolinite cementation could be started at the late eo-diogenitic phase and continued in meso-diagenesis. Kaolinite might have been transformed into dickite, which was recorded locally as traces of pore-filling dickite (Fig. 10 c, d, e, and f). With burial depth and temperature increase, the Illite crystals were formed in a hairy-like texture (Fig. 11e and f). Pore-filling chlorite cement occurred as a replacement for detrital clays. It showed a semi-rosette pattern of crystallization. The high

abundance of kaolinite suggested that chlorite crystals were a by-product of the kaolinite chloritization meso-diagenetic process, together with calcite and CO_2, and siderite could be the source of Fe for this reaction (Worden and Morad, 2003 and references therein). The latest stages of meso-diagenesis were observed by the presence of hydrocarbon emplacement with minor barite cementation.

3.5. Porosity-permeability transform

After characterizing the reservoir heterogeneities on different scales, these properties need to be represented practically. The best reservoir property to describe its characteristic behavior is permeability. Permeability is originally obtained through laboratory core analysis (Slatt, 2006). In the work done by Farouk et al. (2021), core analysis was integrated with thin section, SEM, and wireline logs to infer key petrophysical properties and reservoir quality in terms of storage capacity and hydraulic flow potential, which is usually done to detect the permeability anisotropy in the reservoir. In our case, the lack of core data raised another constraint to estimating the permeability accurately in the form of a continuous property (Shi et al., 2020). Accordingly, a workaround was followed to manage this data gap. In this workflow, formation pressure and fluid samples were used to correlate oil mobility as a fluid property and facies permeability as a rock property. Both were acquired by downhole Formation Tester Tools (RDT or MDT).

An unorthodox method was used to convert the measured mobility into effective permeability. As the mobility values characterize the flowing capability of fluid in a porous medium, thus the higher the mobility, the better the flow capacity will be (Shi et al., 2020). The mobility points were available in 5 NEAG-2 wells in the West segment and two wells in the East segment. Through analyzing the mobility data in the seven wells, 147 values covered the reservoir section to correspond with a porosity value from the well logs. Then mobilities were converted to effective permeability using a viscosity (μ) value for the field oil type (μ=0.87 cP).

Since mobility is the rock permeability divided by the oil viscosity (Shi et al., 2020), the product of mobility and viscosity of the oil will give the permeability Eq. (1).

$$\text{Mobility } (M) = \frac{\text{Permeability } (k)}{\text{Viscosity } (\mu)} \qquad (1)$$
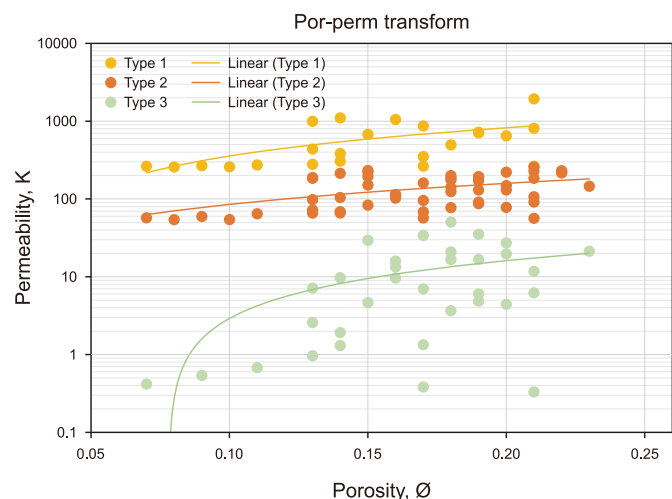
Theoretically, this would give a representative estimate for the actual different facies' permeability and its correlation with the porosity in a linear relationship. A permeability cut-off was applied to separate various facies qualities. As in Fig. 12, different Por-Perm linear relations were created between the calculated permeability and the actual porosity values. Interestingly, it was found that several permeability values corresponded to the same porosity (Fig. 12). A column of different permeability was created on the y-axis, corresponding to the same value on the x-axis. This por-perm cross plot supported the multiple facies model of the reservoir and represented each facies type as a different flow unit as expressed by Eqs. (2)–(4).

$$\text{Log (Perm)} = 1.5687(\text{Por}) + 2.4674 \qquad \text{Facies Type 1} \qquad (2)$$

$$\text{Log (Perm)} = 3.0578(\text{Por}) + 1.5558 \qquad \text{Facies Type 2} \qquad (3)$$

$$\text{Log (Perm)} = 13.059(\text{Por}) - 1.5397 \qquad \text{Facies Type 3} \qquad (4)$$

3.6. Pressure analysis

The field-wide performance should affirm the above-defined reservoir characters. Pressure measurements help define pressure variations among formation intervals, gradients of fluid pressure, fluid contacts, and characterization (Dake, 1983). Pressure analysis in NEAG 2 was conducted to differentiate the reservoir system components and describe different field compartments (West and East segments). Given that the reservoir interval is in an equilibrium state with the underlying aquifer, the pore pressure is expected to increase with depth. The pressure would increase at the hydrocarbon saturated interval with a steeper gradient than the water gradient of the aquifer (Hartmann and Beaumont, 1999). In this workflow, the pressure points in 4 wells in the west and two wells in the east segment were utilized, and then a pressure versus depth linear relationship was created for each well. The pressure range was plotted on the x-axis, and depths were plotted on the y-axis; points of H-C saturated intervals are colored in red. In contrast, those points in the water zone (100% water saturation) are colored blue. Two fluid phases were differentiated from the first well in the segment NEAG 2−1 well. The oil phase pressure gradient was estimated in Eq. (5), while the water phase gradient was estimated in Eq. (6). The intersection point between the oil and water gradient lines is the initial fluid contact in the segment, which is the free water level (FWL) at 2625 TVDSS.

$$\text{Oil gradient } y = 0.9711x - 1184.9 \qquad (5)$$

$$\text{Water gradient } y = 0.6472x + 85.395 \qquad (6)$$

On the other hand, for the NEAG 2 East segment, the free water level was estimated from the first well in the segment NEAG 2E-1. The oil phase gradient showed a very steep gradient Eq. (7), with an over-pressurised point reaching 4234 Psi, while the water gradient of a gentler slope Eq. (8) showed a homogeneous trend. The FWL was estimated at the intersection point between the 2 gradients at a depth of 2631 TVDSS.

$$\text{Oil gradient } y = 1.1661x - 1940.5 \qquad (7)$$

Fig. 12. Semi-log chart plotting the calculated permeability values versus the measured porosity values; a linear transform represents each facies type.

Water gradient $y = 0.6521x + 74.944$ (8)

3.7. Production performance analysis

In this workflow, a decline curve was created for a type well in the West Segment (NEAG 2-4St) and another type well in the East Segment (NEAG 2E-1). On a semi-log plot, the oil, the water, and the total production rate were plotted on the Y-axis versus the timeline of the well production (Production history) on the X-axis. In NEAG 2-4 St well, the total production curve (Grey line) tended to be flat (Fig. 13a). While NEAG 2E-1 well production rate had decreased significantly in a short time (Fig. 13b). Comparing NEAG 2-4St with NEAG 2E-1, the intersection between the water and oil production trend lines is 4000 bbl/d and 250 bbl/d, respectively. This variation reflected a significant difference in the aquifer pressure support.

4. Results

Seven workflows were applied in a sequence from the largest to the smallest scale. The output from a workflow was used in the following one. Several findings were pointed out from each workflow till the overall picture of the reservoir characters was accomplished.

4.1. Regional versus local tectonostratigraphic settings

From the chronostratigraphy analysis, the doubtable boundary between Bahariya bottom and top of Kharita was not confirmed or well defined from both wells. Accordingly, it will be considered a diachronous timeline. Generally, it has been defined on a lithological basis, which is the change from kaolinitic clean sand of Kharita Fm. to glauconitic shaley sand of Bahariya Fm., as previously mentioned. From the Palynofacies analysis (SENV, 2009), the low proportion of marine taxa suggested a marginal marine environment for the Bahariya-Kharita reservoir. The top of Masajid was defined from the deepest point of penetration in the field. It was found to occur below the Kharita Formation, remarking a stratigraphic gap.

To represent the above results in a comprehensive chart, the chronostratigraphic data was imported into the Stratigraphic window in Petrel Software. The stratigraphic sequence and relationships in NEAG 2 Field were compared to the typical

stratigraphic column of Abu Gharadig Basin, as in Fig. 14. In the chronostratigraphic chart of NEAG 2 Field, the log response of the different reservoir zones was also represented. The general trend of the log response showed a fining upward transgressive sequence, with an upward increase in the shale content.

4.2. Fracture-density distribution

The fracture distribution in each well was displayed as strike arrows with dip angle and azimuth direction (Fig. 15). The fracture occurrence was compared to; the lithology (carbonate, shale, or sand), sand quality (average porosity), bed thickness, and the well location to qualitatively define the geological factors controlling it. The distribution of these fractures with depth is illustrated in Fig. 15, where the minor faults are colored in dark blue, possible faults are colored in light blue, conductive fractures are colored in blue, and resistive fractures are colored yellow.

In the carbonate zones (AR/F and IBL), the beds showed a brittle strain response, as they are the highly fractured zones in the three wells. Most of the encountered fractures are resistive, with some conductive/semi-conductive fractures in the WBM wells. NEAG 2-4St well is more heavily fractured than the other two wells, which encountered two fracture networks of resistive and conductive responses through the carbonate beds. Moreover, it encountered several minor faults following the structural field trends (NW-SE and ENE-WSW). It is worth noticing that NEAG 2-4St well is located at the upmost location, NEAG 2E-1 well comes in the second crestal position but in the East segment, and then NEAG 2−5 well is considered at the flank. It suggested that the reason behind this high structuration could be due to the well location at the up-most crestal position in the field, as in Fig. 15.

In Lower Bahariya shaley zones (L. Bah-4 and L. Bah-2), where the dominant lithology is shale with thin sand lenses, they displayed much less frequency of fracture distribution. Virtually no fractures occur in pure shale intervals. All fractures are resistive; small fracture networks were detected in the lime and sand lenses of the L. Bah-4 and L. Bah-2 intervals. In addition, four minor faults were encountered in the L. Bah-4 Zone, of which three minor faults were found in the NEAG 2-4St well.

The fractures increased in sand zones (L. Bah-3, L. Bah-1, and Kharita), where the sand is cleaner (low shale content) and with high average porosity values. Fractures were more frequent in the low-porosity (more brittle) sand beds, as seen in L.Bah-3 sand of NEAG 2-E1. From NEAG 2-4St well, a relation arose between the fracture distribution and the bed thickness, in which most of the
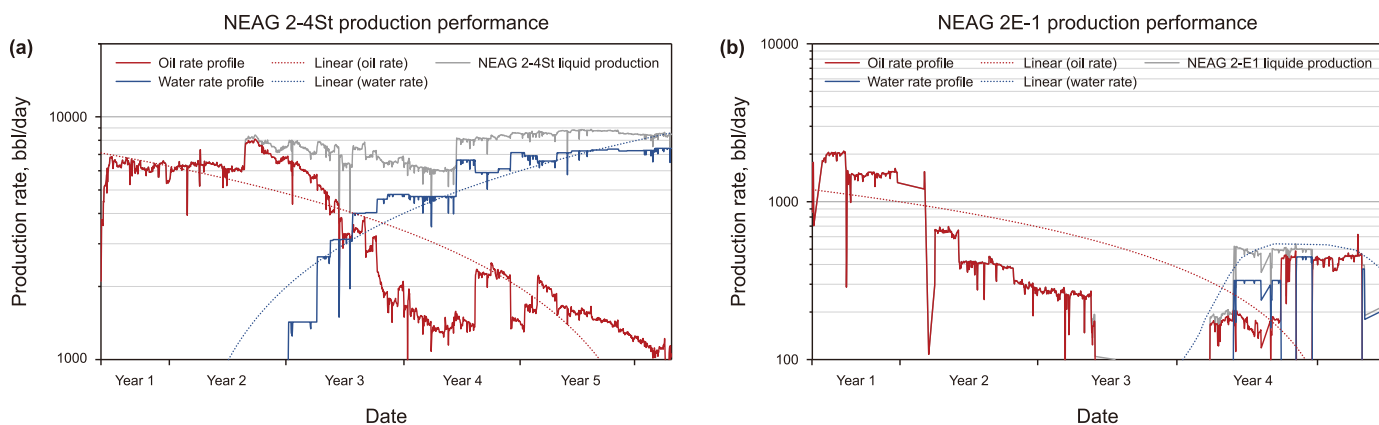
Fig. 13. Production profiles of NEAG 2-4St and NEAG 2E 1 wells, the production rate in (bbl/d) is tracked with time. **(a)** The total production rate (grey line) remains almost flat during the production period, without pressure depletion. **(b)** The total production rate (grey line) sharply declined during the production period, with a significant pressure depletion.
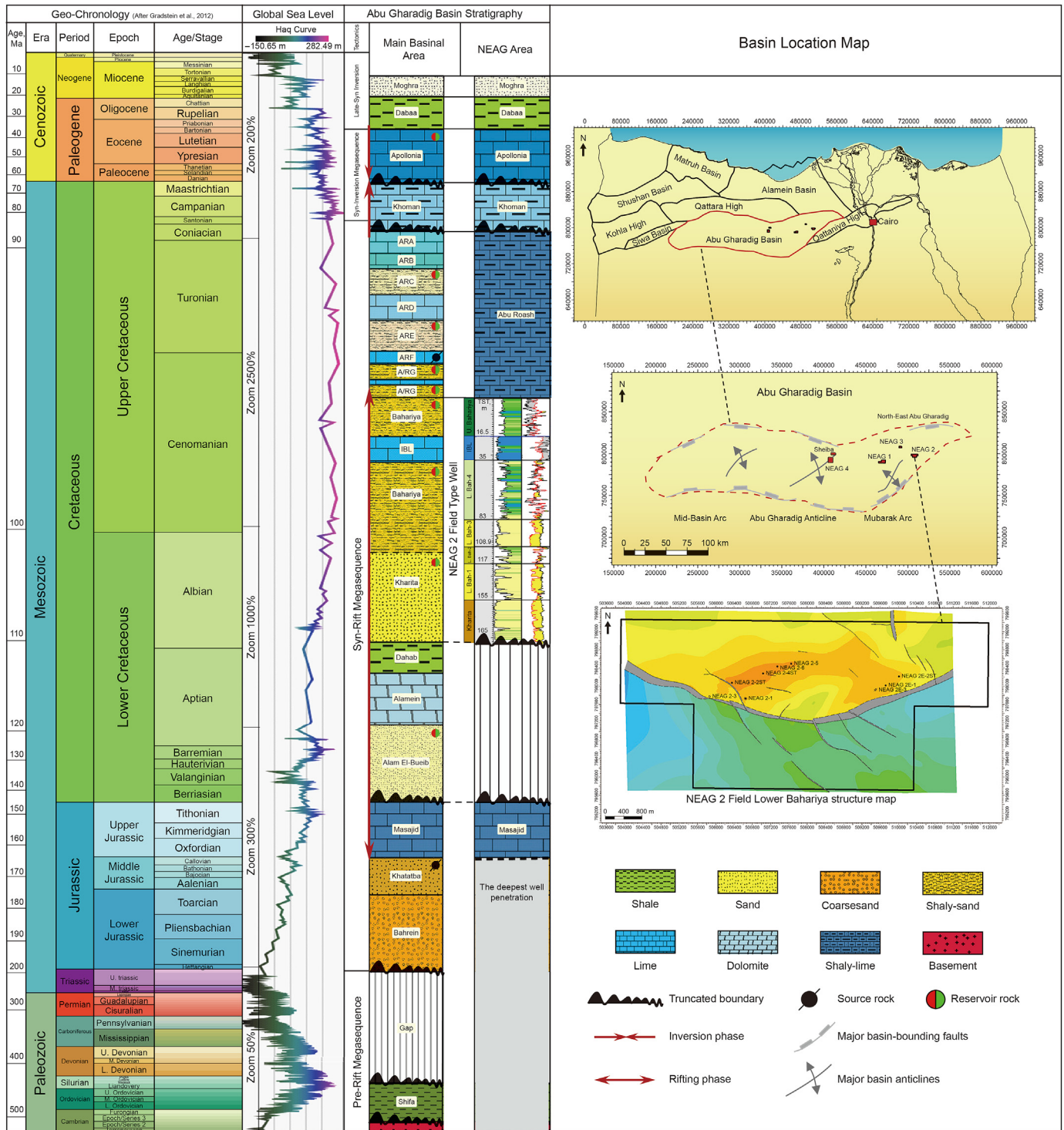
Fig. 14. Abu El-Gharadig Basin regional tectonostratigraphic framework, the basin stratigraphy is referenced to the global sea-level curve, and compared with NEAG 2 Field stratigraphy. It describes the encountered section in the field, the reservoir section zonation, and their log response. The vertical scale is not unified, and the formation's thicknesses are not represented. The basin stratigraphy is compiled from; EGPC (1992), Schlumberger (1995), and Wahdan et al. (1996). The Geologic timescale is according to Gradstein et al. (2012) (Exported from Petrel, 2017). The regional map is compiled from Bosworth and Tari (2021) and references therein. The field structure trends are compared to the regional trends, the NE-SW closure in the field is following the trend of the basinal major anticlinal arches.

fractures targeted the thin or discontinuous sand bodies (Fig. 15). Remarking the top of Kharita zone is the occurrence of a massive network of resistive/conductive fractures and minor faults in the three wells. It is worth mentioning that, regularly, Kharita is differentiated from Bahariya zones by the clay content. Bahariya is

dominated by glaucony pellets, which act as ductile particles that increase their ductility. In contrast, Kharita is a kaolinitic sandstone of brittle behavior, making it more prone to faulting and fracturing, as seen from the image log interpretation.
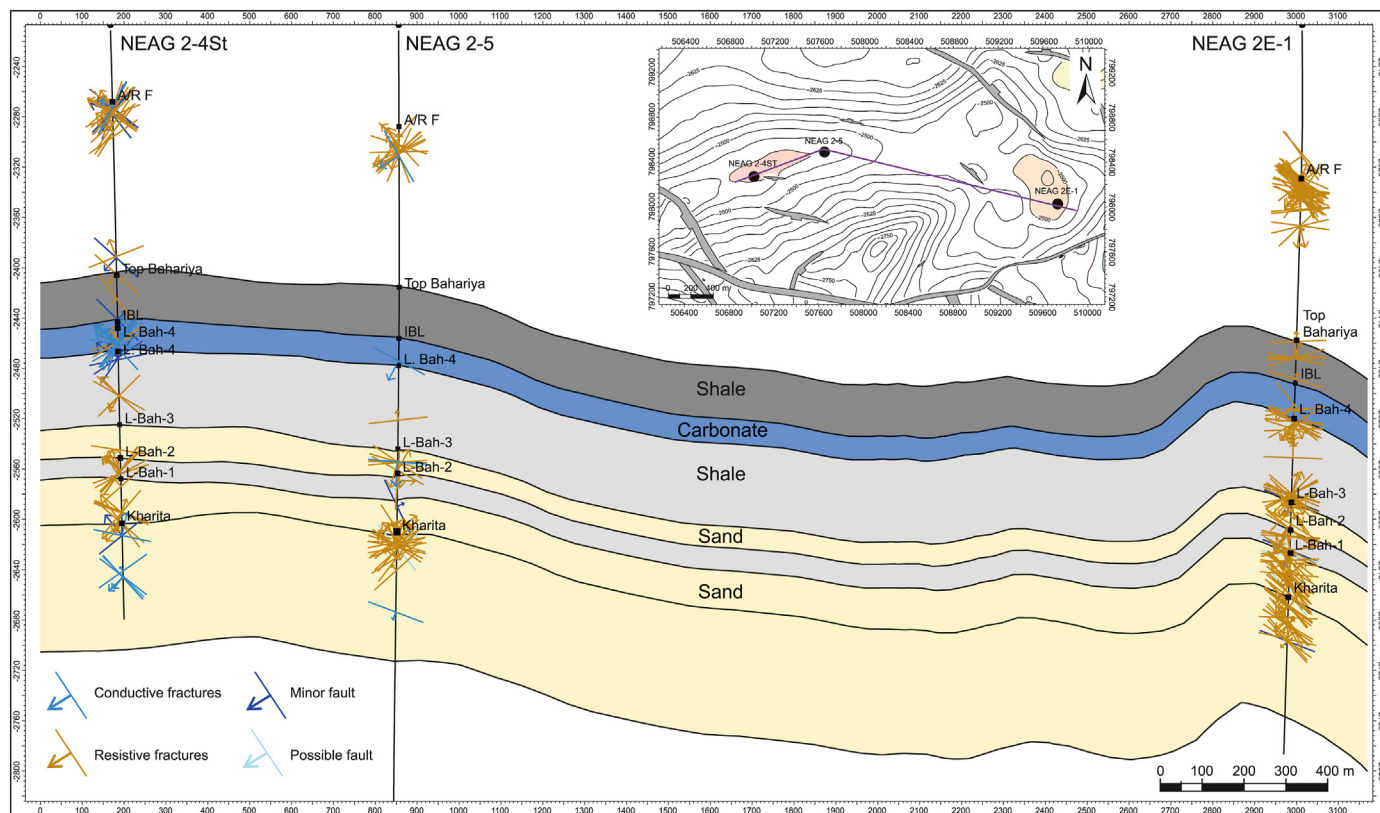
Fig. 15. The fracture density distribution is displayed on a cross-section window for NEAG 2-4St, NEAG 2–5, and NEAG 2E-1 arbitrary lines. The resistive and conductive fractures, minor and possible faults, are displayed at their corresponding depths (Exported from Petrel, 2017).

4.3. Lower Bahariya-Kharita conceptual model

After reporting the facies associations in different reservoir zones described in Schlumberger (2015b), the Lower Bahariya-Kharita conceptual model was created based on the report's findings. In the context of the relationships between sediment supply, accommodation space, and eustatic sea-level fluctuations, the depositional settings of the reservoir system were outlined as a hierarchy of depositional processes (Fig. 16).

The Albian *Kharita zone* represents a coastal plain with fluvial channels depositional system with a tidal influence. This zone shows a massive influx of kaolinitic sandstones from fluvial channels. In contrast, the sandstones of relatively lower quality were deposited in the distributary channels of the distal portion (Schlumberger, 2015b). Allen (1991) initially defined the fluvial-tidal transitional setting as the area between the seaward limit of tidal flow reversal during high river discharge and the landward limit of flow reversal during low river discharge.

The Early Cenomanian Lower-Bahariya zones comprised different depositional regimes developed through consequent flooding events. The Lower part of the Bahariya Formation represents a filling of the sizeable estuarine embayment overlying the Kharita Formation. Dalrymple et al. (1992) defined tide-dominated estuaries as those whose sediment dynamics are driven by tidal currents at the mouth. The upper part of the tidal channels is occasionally topped by tidal flat facies associations, which display flaser and wavy bedding sandstone. The ideal setting of a tide-dominated estuary morpho-sedimentary distribution is a well-defined funnel shape with a mode of tidal wave propagation consisting of longitudinal tidal bars near the mouth, followed by a sandy tidal channel-and-bars complex (Tesseir, 2012), as displayed

in Fig. 16b.

In correspondence to the eustatic sea-level rise, Lower Bahariya zones (1 and 3) comprised glauconitic fining-upward tidal channel sandstones and coarsening-upward subtidal sand bars (Schlumberger, 2015b). The latter was deposited as longitudinal bars along with the channel progradation directions. These sandstone packages were scoured and deposited in an estuarine mudstone background facies deposited as a suspension load during low-energy conditions. The deposits at the upper part of the Bahariya Formation elucidated an upward increase in marine processes, where shelfal shale and carbonate prevailed. *L. Bah-1* comprises the most significant proportions of channelized sand, unlike *L. Bah-3,* which includes tidal channels of smaller dimensions and sand bars (Fig. 16a). While L. *Bah-2* represents the flooding phase of low current strength, sand is either formed in tidal bars or sandy tidal flats. The inconspicuous flat area located seaward of the mudflats and near the tidal channels (Fig. 16b) is occupied by sand flats or mixed (sand-mud) flats. Pure sand sheets (sand flats) or thin sand layers alternating with mud (mixed flats) could be formed when the sand transported in the channels spilled over (Einsele, 2000). The prevalence of mud drapes and mudstone interlayers in the inner estuary suggests that both tidal and fluvial were at low energy (Pontén and Plink-Björklund, 2009). The uppermost L.*Bah-4 Zone* noted the cease of sand supply and prevalence of shelfal shale, which indicates a continuous rise of sea level and an increase in the accommodation space. The sand facies of lower quality and small dimensions were interpreted as transgressive sandstones. These are occasionally recorded in shelfal shale background and suggest deposition during episodic high-energy (storms) conditions (Schlumberger, 2015b). Middle-Cenomanian Intra-Bahariya Limestone *(IBL)* indicates the
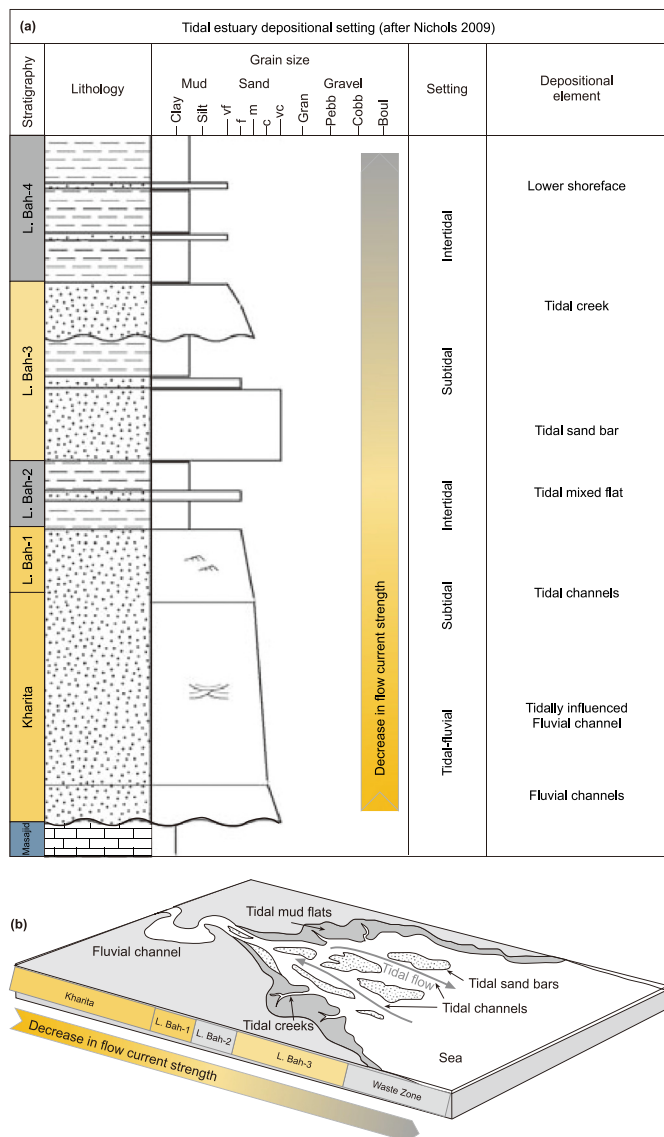
Fig. 16. The distribution of sedimentary bodies and facies in plan and section views, **(a)** A graphic sedimentary log describes the stratigraphic framework of the NEAG 2 reservoir system, adapted from the sedimentary log of a tidal estuary (Modified after Nichols (2009)). Kharita lies unconformably on Masajid at the bottom, and Lower Bahariya zones are displayed with their dominant lithology. The yellow arrow represents the upward decrease in the depositing current strength. **(b)** Tidal-influenced shallow marine transitional depositional setting (Modified after Nichols (2009)), correlated with the reservoir zones to show the distribution of the depositional facies from fluvial channels, tidal channels, tidal bars, and flats.

submergence of the area by the marine waters in correspondence to the peak of sea-level rise.

4.4. Electrofacies log

In the well-section view (Fig. 17), the input classification curve (Facies Code) was displayed versus the output classification IPSOM curve for comparison and model correlation. The model seemed to reasonably correlate with the input interpretation for the three wells incorporated in the model as control points (NEAG 2-4St, NEAG 2-5, and NEAG 2-E1). Since the petrophysical logs were used for learning facies differentiation (whose sample rate is finer than the image interpretation), the resulting classification IPSOM captured the small-scale variations in logs response, i.e., detailed

facies typing. The model is then applied to the other wells (Grey headers) to create classification curves for all field wells (Fig. 18). The generated classification curve depicts the reservoir system evolution as a story-telling sequence of events. The overall sequence is a transgressive depositional sequence, starting at the *Kharita* level with continental facies (dominant Type facies 1). Followed by continental facies with subordinate tidal influence (Type 1 and 2), it continued from the tidal setting to the estuarine embayment setting, up to the shallow marine sandy shale and sand facies (Type 1, 2, and 3) in Lower Bahariya zones. It was finally topped by the massive, widely extensive carbonate bed of *IBL*.

The electrofacies logs interestingly reflected the evolution of the depositional setting from continental to transitional (Fig. 18). This correlation panel adequately explained the facies variation between closely spaced wells. For example, in the upper zone (L. Bah-3) in NEAG 2-4St well, the good quality sand died out in the east direction. This sand disappearance is because L. Bah-3 comprises three well-developed sand bodies (Type 1, 2, and 3), but Type 2 and Type 3 have limited lateral extensions. This explanation was supported by the next offset well (NEAG 2-6), which encountered smaller thicknesses of (Types 1, 2, and 3). Consequently, further to the east, the NEAG 2-5 well was solely dominated by shaley sand (Type 3), while the other facies types were not extended to the NEAG 2-5 well location (Fig. 18). This result justified the facies variation in L. Bah-3 recorded in the facies analysis.

4.5. Reservoir quality modifiers

The identified diagenetic processes have decreased or increased the effective porosity and, therefore, downgraded or enhanced reservoir quality. The tight to good reservoir qualities are usually attributed to the local effects of the diagenetic processes with variable degrees (El Hossainy et al., 2021). Infiltration of detrital clays, carbonate and silica cement, quartz, and feldspar overgrowths was acting to decrease the pore volume, not to mention the profound effect of mechanical compaction on porosity loss. These processes would be considered the main reasons for porosity reduction. On the other hand, porosity enhancement could be counted for partial to complete dissolution of feldspars and glaucony. Dissolution of carbonate cement and dolomitization, and to some extent, micro fracturing, enhanced the porosity. Ideally, fractures improve the permeability of any sandstone reservoir (Hartmann and Beaumont, 1999). In NEAG-2, Fractures were the primary factor in improving the permeability of sandstone reservoirs with low porosity, such as L. Bah-2 and L. Bah-4 zones.

Besides the above processes, the crystallization of authigenic clays (kaolinite, illite, and chlorite) is a critical process with which some parameters should be considered. When dealing with diverse types and habits of clay minerals, each of which would affect the porosity-permeability differently (Hartmann and Beaumont, 1999; Ulmer-Scholle et al., 2016; Worden and Morad, 2003 and references therein). The paragenesis graph reveals that clays are mutually intergrown and contain a wide range of solid solutions. Likewise, they are formed by different depositional and diagenetic processes.

A semi-quantitative chart was created by XRD samples per reservoir zone (Fig. 19), which quantified the main clay mineral types and behaviors in the reservoir system. Kaolinite, illite, and chlorite are the key players in the reservoir pore system, and mixed layer (illite-smectite) clays were detected only in NEAG 2E-1 well (Fig. 19c). The dominant clay type recorded in all zones was the kaolinite (40%–90% of clay size fraction); illite came in second place. In comparison, chlorite was detected occasionally at various depths but did not exceed (27% of the clay size fraction). In the NEAG 2E-1 well, illite-smectite was detected in 3 samples at L. Bah-3 and Kharita zones, which should remark a different reservoir
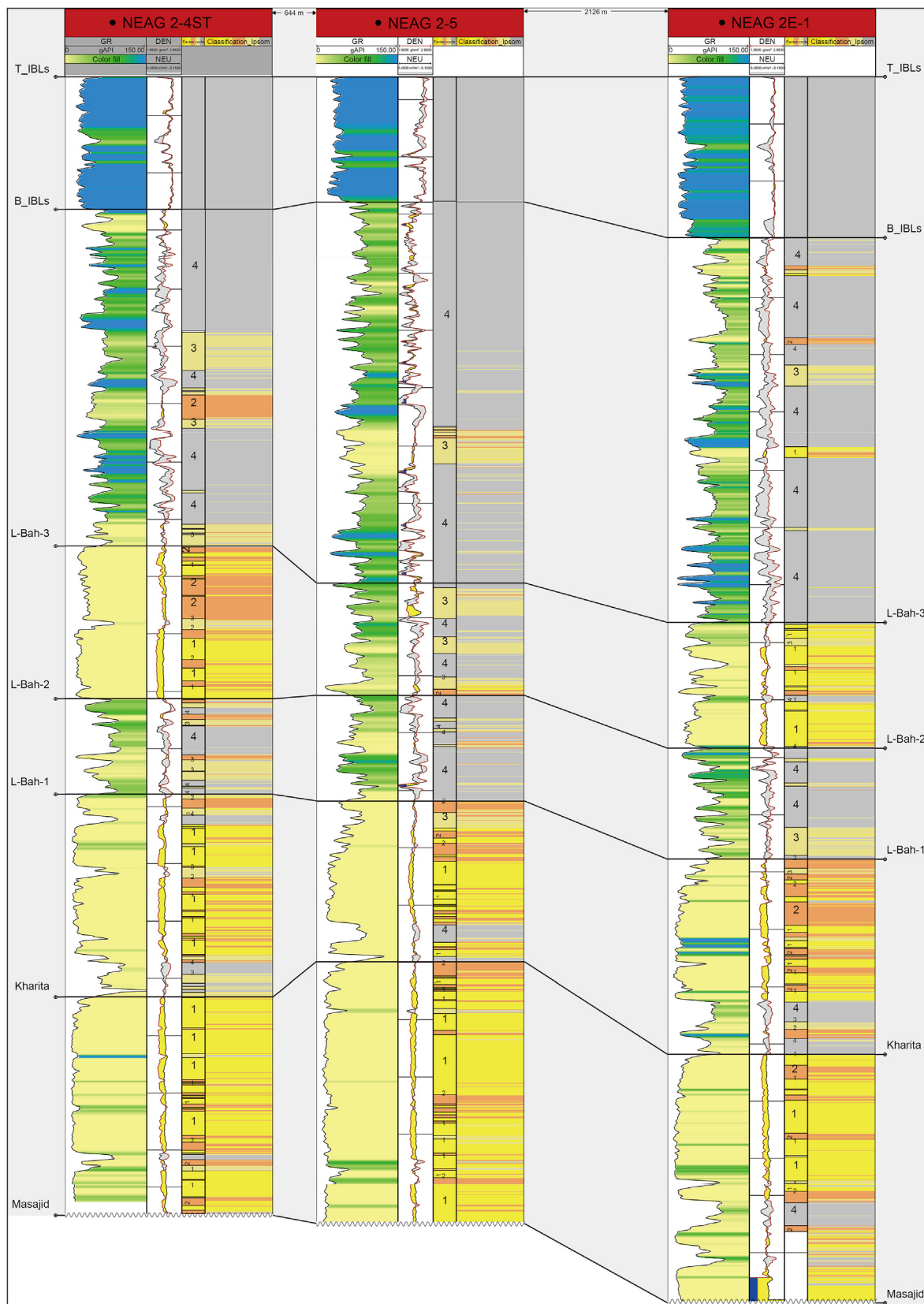
Fig. 17. A well-section window displays the 3 control point wells (NEAG 2-4St, NEAG 2-5, and NEAG 2E-1), with GR, DEN/NEU, input Facies Code and output Classification IPSOM logs, respectively (Exported from Petrel, 2017).
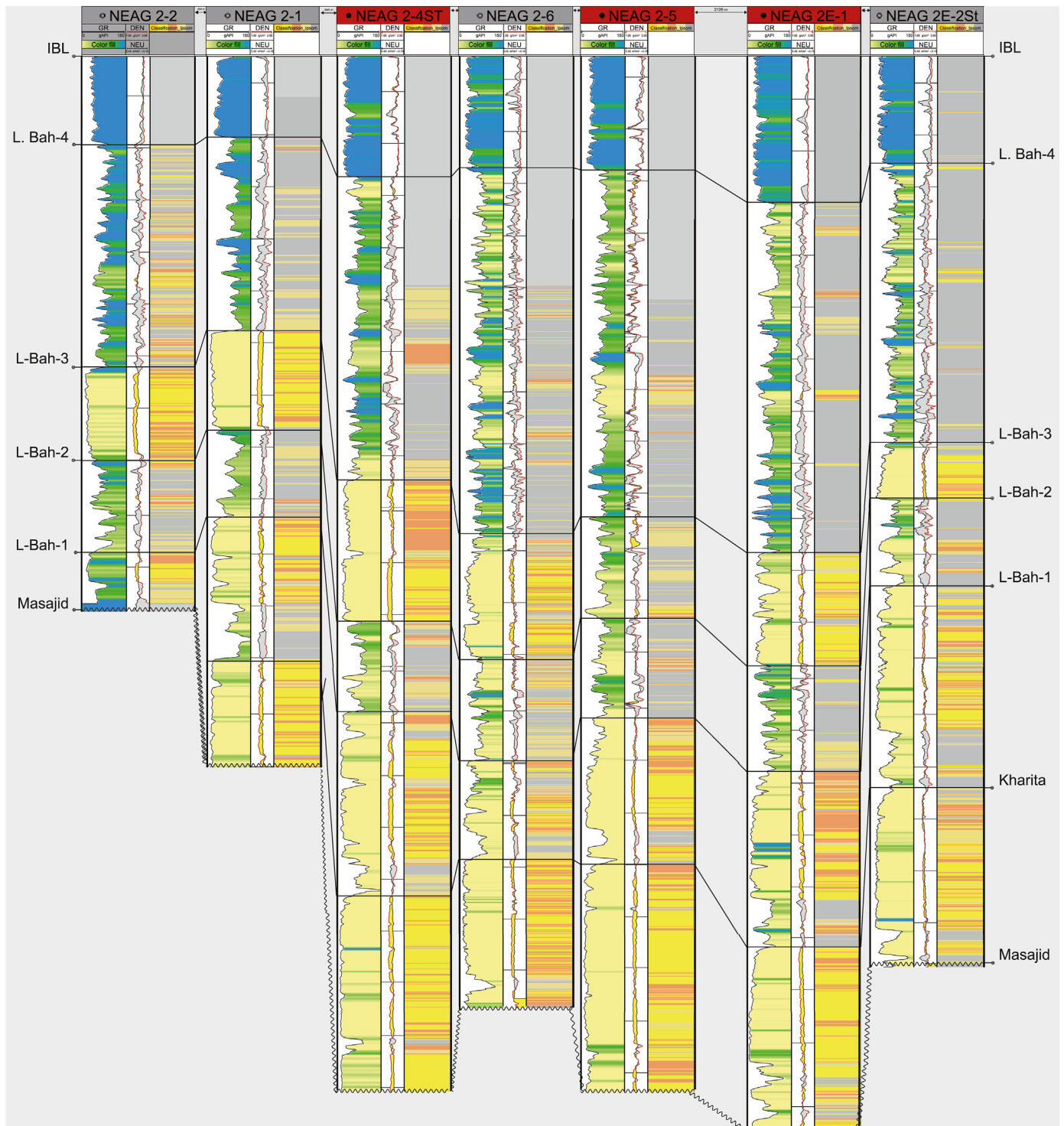
Fig. 18. A well-section window displays the model after application on all field wells. The offset wells (NEAG 2-2, NEAG 2-1, NEAG 2-4St, NEAG 2-6, NEAG 2-5, 2E-1, and NEAG 2E-2St) are colored in grey. The control point wells (NEAG 2-4St, NEAG 2-5, and NEAG 2E-1) are colored in red. The correlation is flattened on top (IBL) as the top datum to remove the structure elevation; the well spacings are also represented. Two general trends could be identified, first: the sand quality and thickness decrease upward. Second: the sand quality and thickness decrease towards the East segment (Exported from Petrel, 2017).

setting in the NEAG 2 East Segment from the West Segment. Therefore, the types and mode of occurrence of clay minerals found in NEAG 2 could be correlated with the facies types, i.e., qualities. The SEM images gave a good insight into the clay mineral's habits (Fig. 11). By integrating the SEM images with the XRD points and the E-Facies logs in Petrel Software, the dominance of each clay

mineral was correlated with different Facies types, this came out with some exciting findings listed as follows:

Kaolinite was found as a pore-filling vermicular, delicate booklet with an accordion-like texture. It was correlated to Facies Type 1, in which the best quality would be expected (Fig. 19a) and (Fig. 19b). *Illite* was found with hairy-like textures on detrital clay surfaces,

(a) NEAG 2-4St

(b) NEAG 2-6

(c) NEAG E-1
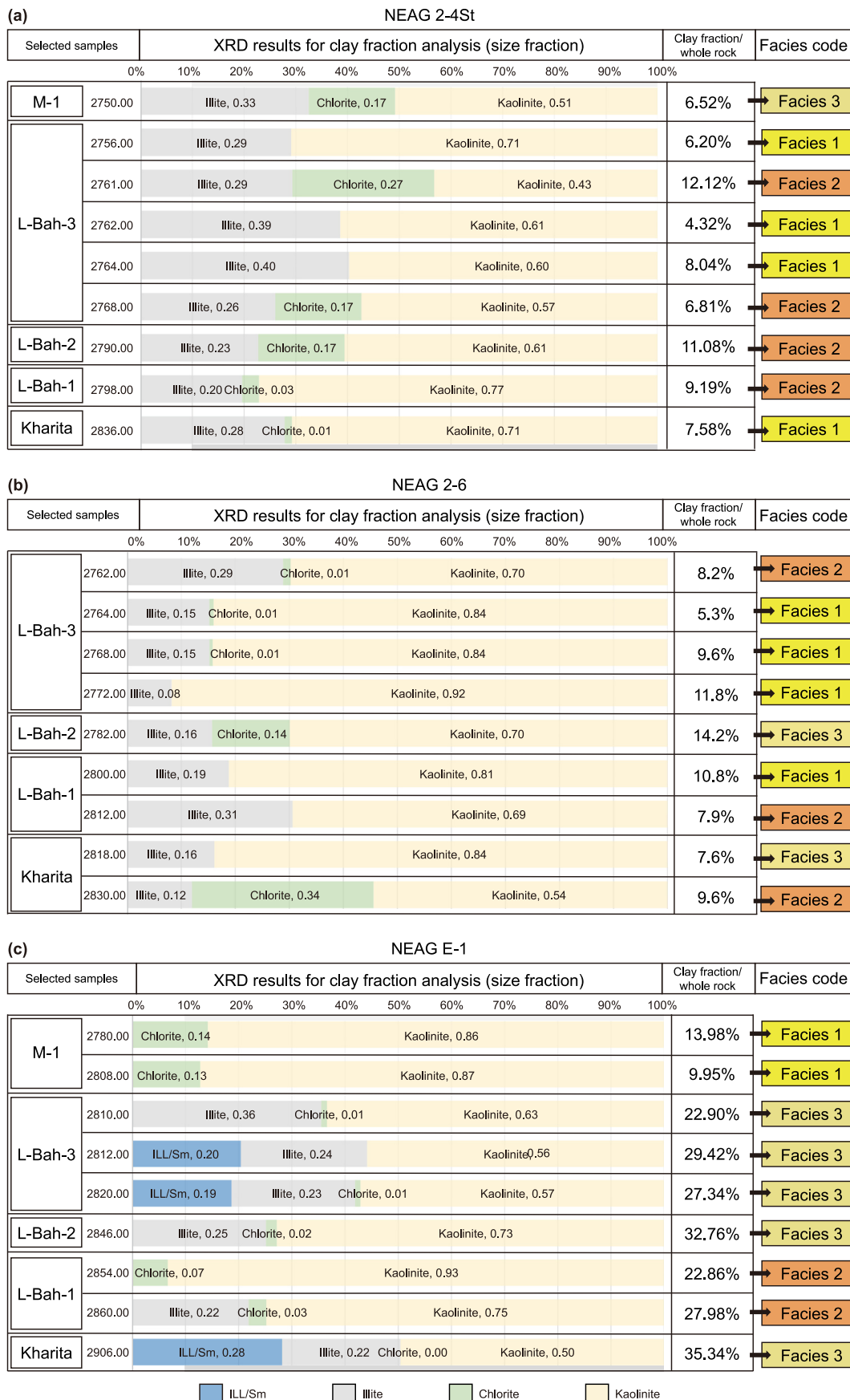
Fig. 19. Quantitative XRD analysis of selected samples from **(a)** NEAG 2-4St, **(b)** NEAG 2–5, and **(c)** NEAG 2E-1, the percentage of clay mineral and the dominant type is correlated to the Electro-facies log.
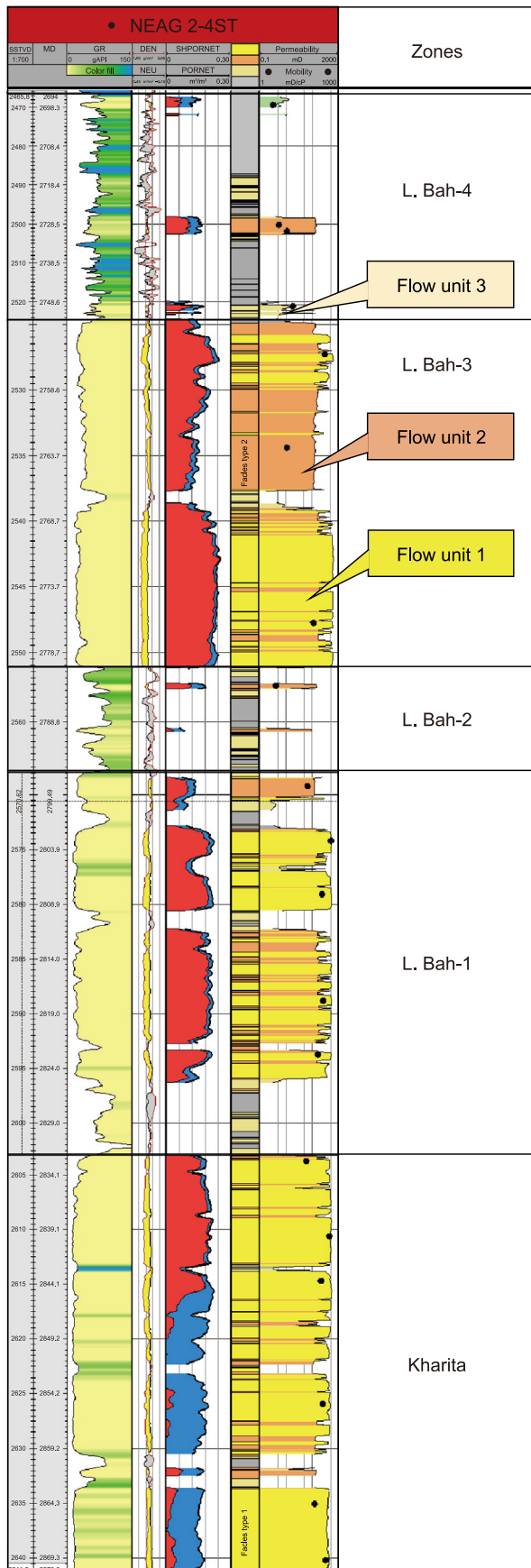
filling pore spaces, which could be related to Facies Type 2 or 3, which is expected to decrease the quality (Fig. 19). *Chlorite* was found as pore-filling and grain-coating authigenic chlorite platelets, rosette pattern on a chlorite-coated detrital quartz grain. In some cases, chlorite was seen as a replacement for detrital clays and showed a semi-rosette pattern (Fig. 19). It was recorded in the 3 facies types but did not exceed 15% in Facies Type 1 (Fig. 19a) and (Fig. 19b). *Illite-Smectite* is a mixed-layer clay mineral resulting from the interstratification of different mineral layers in a single structure (Worden and Morad, 2003 and references therein). It was detected only in NEAG 2E-1 by XRD in trace amount, with no defined morphology. Therefore, it is unclear how it would have affected the facies quality, but as illustrated in (Fig. 19c), it was restricted to Facies Type 2 and 3. As previously noted, glaucony is formed after smectite or illite clay minerals. Therefore, this mixed layer of clays could be correlated with the glauconitic facies, which are expected to have the lowest quality among the others.

4.6. Reservoir flow units

Reservoir systems are subdivided into containers confined in a pore system to understand the reservoir rock-fluid interaction and performance. When fluid is drained, this system comprises one or more flow units that react as one unit (Hartmann and Beaumont, 1999 and references therein). There are four containers in the NEAG 2 reservoir system: L. Bah-4, L. Bah-3, L. Bah-2, L. Bah-1, and Kharita zones. The reservoir flow units are defined based on similar pore types and qualities. The reservoir performance is expected to be different among different flow units (Farrag et al., 2021), therefore, each flow unit should have a specific porosity-permeability relationship, by which the reservoir characteristics are defined and reservoir performance can be predicted.

Ideally, the hydraulic flow units would be defined by the automated reservoir zonation method which subdivides the reservoir into petrophysical classes (HFU) that represent varying flow and storage capacities (Jafarian et al., 2024). In the case of core unavailability, we had to use the por-perm transforms created in Section 4.5, to integrate it with pre-generated electro-facies logs from the IPSOM module to delineate reservoir flow units. A specific por-perm transform equation was applied per each facies type. As a result, a permeability curve was created in Petrel Software and conditioned to the Electro-facies log using a (Perm) equation per facies type (Section 3.5, Eqs. (2)–(4)). For example, the por-perm transform (1) was applied to Facies type 1 (the highest quality rock type), and por-perm transform (3) was applied to Facies type 3 (the lowest quality rock type). The resultant log is displayed as a permeability curve filled with the colors of the three reservoir facies types to validate the correlation between the facies types (quality) and their permeabilities i.e. flow behavior, as in Fig. 20. By this way we can say that the reservoir has three facies types, each has its permeability range, which reflects its flow behavior and can be considered as definite flow unit.

4.7. Reservoir system components

The water-hydrocarbon system enclosed inside the pores of a rock unit is referred to as a reservoir system, arranged as a waste zone, a reservoir, an aquifer, and a transition zone (Hartmann and Beaumont, 1999). It is not essential to find the four components in every reservoir system; they vary in dimensions and properties

Fig. 20. NEAG 2-4St well displayed as the field type well. The Permeability curve was created by applying 3 different transforms conditioned by the pre-created Electro-facies types. Three flow units are differentiated according to the corresponding facies type (Exported from Petrel, 2017).
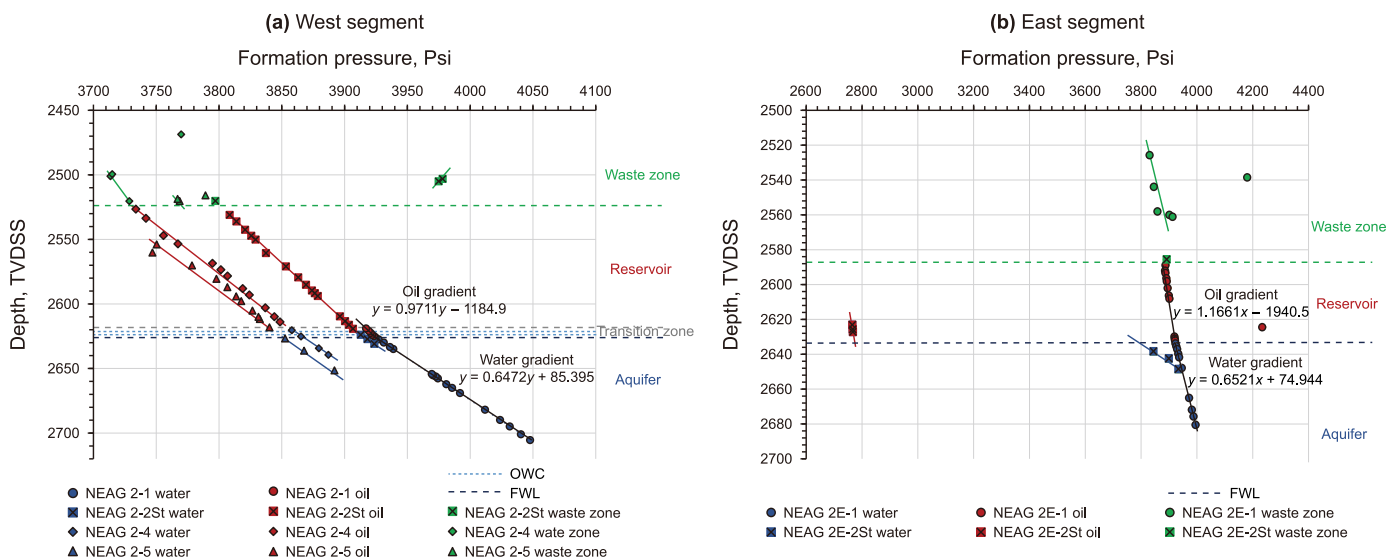
Fig. 21. A pressure analysis chart for the West and East segments, in which the formation pressure points are plotted versus depth to identify different reservoir system components (Aquifer, Transition, Reservoir, and Waste zones).

from one system to another. The product of the pressure analysis was the description and definition of each reservoir system component.

In Fig. 21a, the interval below FWL depth (2625 TVDSS in the West segments) is the reservoir system aquifer corresponding to the Kharita container. From the following development wells in the West segment, NEAG 2-2St, NEAG 2-4St, and NEAG 2-5, minor pressure depletion <200Psi was observed. The pressure depletion for such wells producing at high rates is considered insignificant, prohibiting the ability to delineate the reservoir connectivity. The water level was recorded at different depths, fluctuating up and down above the FWL. From NEAG 2-1, the water contact was recorded from the logs at 2625 TVDSS. In NEAG 2-2St, the water-front was at 2621 TVDSS; then in NEAG 2-4St, it was at 2615 TVDSS. At last, NEAG 2-5 was recorded at 2621 TVDSS, which returned at the same depth recorded in NEAG 2-2St. This fluctuation is called the waterfront movement (light blue dashes), within which the transition zone could be outlined (Fig. 21a). At the shallowest depths, another pressure attitude was recorded; most points (colored in green) were over-pressured and scattered, and no definite gradient could have been drawn. This overpressure means the sand bodies are of low permeability and do not communicate with each other at this interval. Concluding that this could represent the waste zone of the reservoir system in NEAG 2 West segment. The waste zone corresponded to L. Bah-4, which by definition lies below the cap rock (IBL), is over-pressured, and of low-quality facies.

In Fig. 21b, the interval below FWL depth (2631 TVDSS in the East segments) is the reservoir system aquifer corresponding to the Kharita zone container. Unlike the West segment, the second well in the segment NEAG 2E-2St showed a significant pressure depletion >1000 Psi at the perforated intervals. Since the East wells' data was limited, no evident transition zone attitude was recorded. At the shallow intervals, the points were over-pressured for both wells and scattered, with no defined gradient. Resembling the waste zone in the West segment, L. Bah-4 could be considered the waste zone for the reservoir system in the NEAG 2 East segment.

4.8. Reservoir drive mechanisms

The reservoir drive mechanism provides the energy that drives

the hydrocarbon from the reservoir container to the wellbore perforations when hydrocarbon fluid is generated (Hartmann and Beaumont, 1999). The hydrocarbon recovery efficiency can be predicted and estimated by defining the drive mechanism for a given reservoir. The NEAG 2 Reservoir System, is expected to be a water drive mechanism.

Since, in NEAG 2-4 St well, the total production curve was found to be flat; therefore, this is a strong water drive (Fig. 13a). The aquifer's water expands slightly and displaces the oil from the reservoir toward the borehole as pressure drops around the borehole. It provides excellent pressure support from the aquifer (100% voidage replacement), with a minimal pressure drop at the wellbore (Hartmann and Beaumont, 1999). The strong water drive occurs when the aquifer is of equal or better quality than the reservoir and has a much larger volume. This strong aquifer support in the West Segment explains the rapid increase in water production.

On the other hand, in the NEAG 2E-1 well, the production rate decreased significantly in a short time (Fig. 13b). This rapid decrease in the production rate indicated that the aquifer is smaller and has lower quality; there is a limited expansion of water into the reservoir as oil is withdrawn. As the aquifer water support diminishes, the hydrocarbon production rate drops more rapidly than with a strong water drive, and oil recovery is reduced (Hartmann and Beaumont, 1999). As a result, there is a partial water drive in the East Segment, where the water support diminishes with production.

The reservoir system production performance is primarily expressed by the production curve analysis, together with the recovery factor. The oil recovery is reduced as the hydrocarbon production rate drops more rapidly. In the case of the West Segment, the recovery factor is expected to be 45%–60%, while in the East, it would be 30%–45% of the total oil volume, according to Hartmann and Beaumont (1999).

5. Discussion on the reservoir system behavior

After understanding the reservoir system parameters and its multiscale heterogeneities, reservoir behavior still needs to be outlined. The term reservoir behavior is meant to include the production performance with time, the prediction of future productivity, and the common issues required to be handled. The
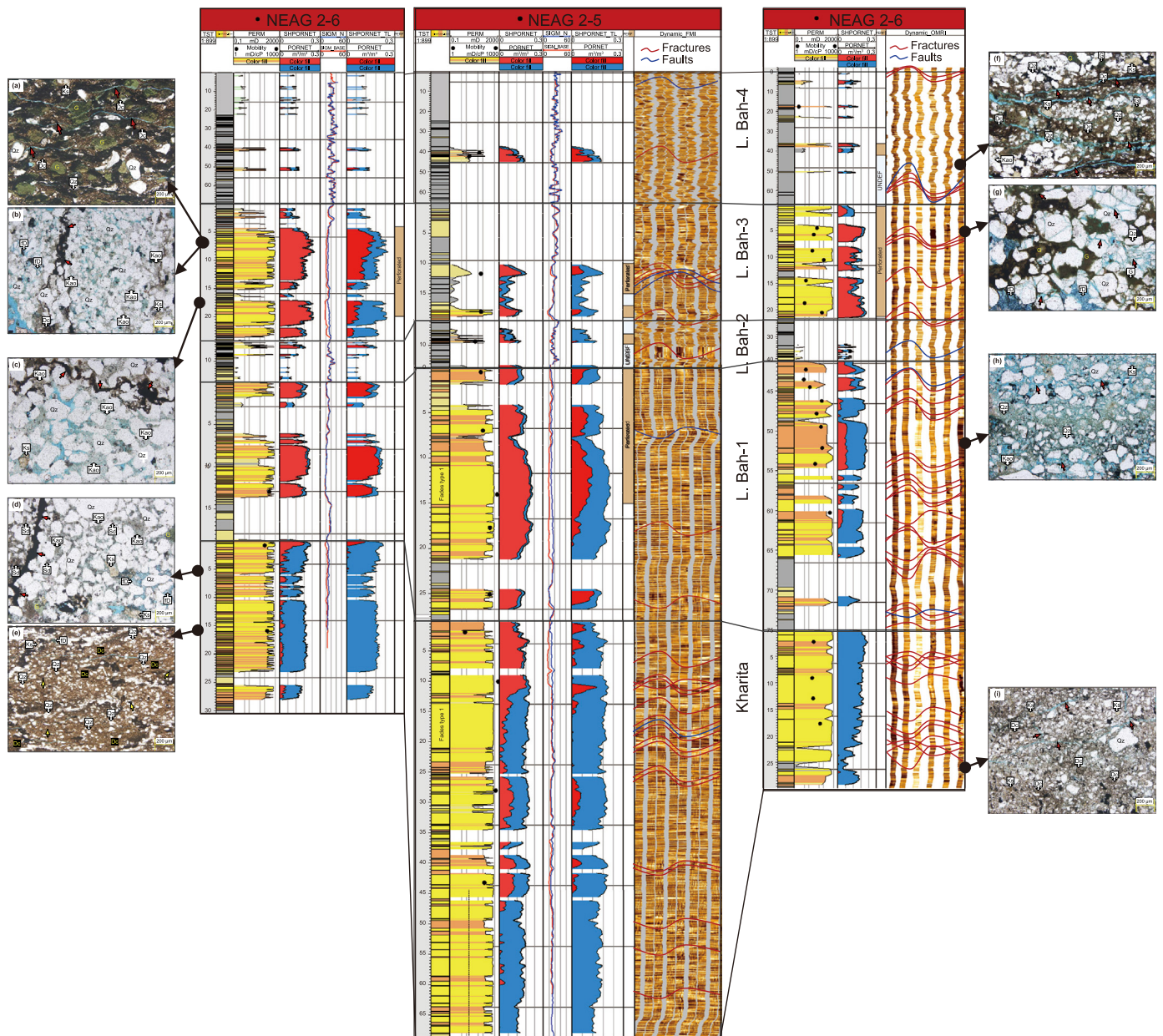
Fig. 22. The final comprehensive reservoir system portrait includes the Electro facies log, Permeability curve (flow units), TDT (ShPornet, Sigma_base, Sigma_N, and ShPornet TL) are displayed with the Perforated intervals and BHI Dynamic logs. In addition to representative thin sections, displayed for selected wells to express the reservoir system characters of different containers and flow units. Note: the faults and fractures dip azimuth and angle are not represented (Exported from Petrel, 2017).

reservoir system characters controls two essential economic elements of a prospect: the rate and the amount of hydrocarbons recovered (Hartmann and Beaumont, 1999). Statically, pore type and pore fluid interaction in different flow units are the most critical elements determining reservoir system performance.

The final reservoir portrait was created by displaying the conventional well logs, image logs, and petrography with the dynamic data to describe the different flow units in the reservoir (Fig. 22). It is clear that the Flow units are well defined on log response, image interpretation, petrographic features, pressure data, permeability curve, and advanced saturation logs (TDT). The Thermal Decay Time log (TDT) was added to the reservoir system behavior chart to compare the water saturation before and after production (Fig. 22). The TDT logs and mobility points could be considered dynamic properties that reflect the fluid flow ability

during production. The mobility points are displayed on the permeability curve, in which each facies type is represented uniquely as a definite flow unit. The planar features from the BHI were analyzed and expressed statistically to identify subsurface fracture zones, weak zones, and zones of subsurface flow. To evaluate the effect of these properties on production behavior, the fracture density was compared with the permeability, mobility values, and TDT logs in front of the opened (perforated) and closed intervals (Fig. 22). By integrating the available data in NEAG 2-6 and NEAG 2-5 West wells and NEAG 2E-1 East well, some data gaps were compensated by other data types. For example, there was no BHI data in NEAG 2-6 well, though the fracture and facies were assessed from the thin section description. No TDT log was acquired in NEAG 2E-1, but the mobility points compensated for it. This integration resulted in a comprehensive reservoir portrait

([Fig. 22](#)), from which several explanations were pointed out.

First, the *Kharita Container* is not perforated in any field well, but most of the oil was drained out, as seen from the TDT log response. Despite the aforementioned shale marker between Kharita and L. Bah-1 sand, Kharita contributed to the production. The zone is densely fractured in the three wells, as recorded from the BHI and thin section description, suggesting a vertical communication between the two containers, leading to the early and rapid water breakthrough and aquifer-reservoir direct communication. Second, *L. Bah-3 Container* showed a variety of facies types. In NEAG 2-6 at the same depth, two different microfacies were identified from the thin section, glauconitic sub-feldspathic wacke and kaolinitic quartz arenite, which was captured by the Electro-facies log. Third, N-5 Well, had high mobility values detected in front of Flow unit 3 of the lowest quality, indicating that the fractures cause these high mobility values at the same spot. The same behavior was observed in NEAG 2E-1 Well but in the L.Bah-4 container dominated by Flow unit 3, in which microfractures were recorded in the thin section in front of the perforated interval. Largely, the NEAG 2E-1 Well showed a different flow unit distribution, fracture density, and fluid contact than the west wells. Supporting the previous findings of the dissimilar reservoir pressure system and drive mechanisms between both segments in the field.

6. Conclusions

Lower Bahariya-Kharita in NEAG 2 Field is a complex-heterogenous reservoir system. The reservoir performance is a function of the number, quality, geometry, and location of containers within a reservoir system, its drive mechanisms, and fluid properties. When performance does not match predictions, any of these variables could be misinterpreted or misrepresented. The dynamic data should be integrated with the geologic data to limit the geologic uncertainties in the created model. The current work achieved a comprehensive reservoir portrait that has given a reliable explanation for most phenomenal reservoir production performances. Such reservoir quality and connected volumes would imply that the aforementioned RF mismatch is due to unrecovered reserves, and a production strategy should be customized to bridge the gap to the TQ RF. The unavailability of core data can be compensated by applying machine learning methods. The innovation in this work is in integrating all types of data describing the multiscale heterogeneities of the reservoir in one sequential workflow and in offering solutions to overcome data gaps. The main conclusions on NEAG 2 reservoir system behavior can be listed as follows:

1 The West and East segments have different reservoir characters, facies distributions, qualities, diagenetic alterations, fracture densities, and structural trends. The reservoir system in each segment has its particular behavior, drive mechanism, and pressure regime.

2 The fracture density increased with decreasing shale content. Carbonates and poor-quality sand are more susceptible to being fractured. For the same lithology, thin beds were more fractured than thicker beds; thus, bed thickness is inversely proportional to fracture density. Regarding the well location, it is expected that the crestal well position caused more fracturing and faulting, favoring high mobility values, best production performance, and early water breakthrough.

3 Facies grouping is mandatory, by which each facies group should have a clear manifestation of its log response to be differentiated by the deep learning technique (Neural Network analysis). The number of facies groups or reservoir rock types should not exceed three types.

4 The Neural Network analysis is the most convenient machine learning method to compensate for the data gaps in the field. The created electro-facies log explained the facies typing, and its variations spatially and temporally. Between the successive wells in the West segment (NEAG 2-4St, NEAG 2-6, and NEAG 2-5) the facies quality decreased laterally towards the east. In the East Segment, the facies distribution and qualities are quite different, dominated by Facies Type 2 and 3 with smaller channels. Generally, the depositing current strength decreased upward in a transgressive depositional sequence and decreased laterally towards the east.

5 Several quality modifiers were identified, with enhancing and decreasing effects on the facies' flow performance. An unorthodox method was applied to create three permeability equations for each flow unit describing its behavior using the mobility values. Despite the method's uncertainty, it has overcome the problem of permeability estimation when no real data from the whole rock core.

6 Different pressure systems have been detected in each segment, Kharita is the reservoir system aquifer, L. Bah-1, L. Bah-2, and L. Bah-3 are the reservoir zones, and L. Bah-4 is the waste zone in both segments. The difference in production performance in each pertained to the different drive mechanisms. The dominating drive mechanism is controlled by the dimension and quality of the aquifer (Kharita Zone), which caused a strong water drive in the West Segment, and a partial water drive in the East Segment.

7 This complexity and heterogeneities must be simulated statically and dynamically to improve the production forecast. For the field production optimization, avoiding the fractured zones close to the oil-water contact is recommended since the fractured aquifer, and the vertically connected zones encouraged the unexpected high water cut. A perforation strategy, such as partial perforation, could be implemented considering the fracture distribution to avoid premature water breakthrough. In addition, each reservoir zone should be revisited for workover opportunities. The waste zone of the system (L. Bah-4) would offer an economic reserve. However, it comprises Flow-unit 2 and Flow-unit 3 of lower qualities; its large thickness and wide existence all over the field should make it economical. Lastly, the uncontrolled area between the West and East Segments of the field should be appraised for further opportunities. Largely, this integration of workflows is highly recommended to be applied to similar cases of multifaceted-complex-heterogeneous reservoirs in nearby fields or basins.

CRediT authorship contribution statement

Ola Rashad: Writing – original draft, Visualization, Software, Methodology, Formal analysis, Conceptualization. **Ahmed Niazy El-Barkooky:** Writing – review & editing, Validation, Supervision. **Abd El-Moneim El-Araby:** Writing – review & editing, Validation, Supervision. **Mohamed El-Tonbary:** Writing – review & editing, Validation, Supervision, Resources.

Declaration of competing interest

The authors declare that they have no known competing financial interests or personal relationships that could have appeared to influence the work reported in this paper.

Nomenclatures

M	Mobility (m/s)/(V/m)
Φ	Por = Porosity (%)
k	Perm = Permeability (md)
μ	Viscosity (cP)

Acronyms and Abbreviations

BBL/D	Barrels per day
BHI	Bore Hole Imaging tools
CAL	Caliper
DEN	Density
E-facies log	Electro-facies log created from the conventional logs
FMI	Fullbore Formation Microimager tool
FWL	Free Water Level
GR	Gamma-ray
IBL	Intra Bahariya Limestone marker
IPSOM module	Application of the artificial neural networks in Techlog Schlumberger software
L. Bah	Lower Bahariya Zone
MDT	Schlumberger Modular Formation Dynamics Tester
NEAG	North East Abu Gharadig Area
NEU	Neutron
NEU	Resistivity
NTG	Net to Gross calculated log
OMRI	Oil Mud Reservoir Imager tool
PEF	Photoelectric factor
PorNet	Net pay porosity calculated log
RDT	Halliburton Reservoir Description Tool
SEM	Scanning Electron Microscopy
SHC	Saturation hydrocarbon calculated log
TDT	Thermal Decay Time log
TQ RF	Top Quartile Recovery Factor
XRD	X-ray diffraction analysis
XRMI	X-tended Range Micro-Imager tool

References

Allen, G.P., 1991. Sedimentary processes and facies in the Gironde estuary: a recent model for macrotidal estuarine systems. AAPG Memoir 16, 29—39.

Al-Moqaddam, R.O., Darwish, M., El-Barkooky, A.N., Clerk, C., 2018. Sedimentary facies analysis of the upper Bahariya sandstone reservoir in East Bahariya C area, North Western Desert, Egypt. Egypt. J. Petrol. 27, 1103—1112. https://doi.org/10.1016/j.ejpe.2018.03.009.

Bosworth, W., Tari, G., 2021. Hydrocarbon accumulation in basins with multiple phases of extension and inversion: examples from the Western Desert (Egypt) and the western Black Sea. Solid Earth 12, 59—77. https://doi.org/10.5194/se-12-59-2021.

Corex, 2019. Petrographic Analysis of NEAG 2 Ditch Cuttings (Unpublished results).

Dake, L.P., 1983. Fundamentals of reservoir engineering. In: Dake, L.P. (Ed.), Fundamentals of Reservoir Engineering. Elsevier.

Dalrymple, R.W., Zaitlin, B.A., Boyd, R., 1992. Estuarine facies models : conceptual basis and stratigraphic implications. J. Sediment. Petrol. 62, 1130—1146. https://doi.org/10.1306/D4267A69-2B26-11D7-8648000102C1865D.

EGPC, 1992. Western Desert, oil and gas fields, a comprehensive overview. 11th Petrol. Explor. Prod. Conf. 1—431.

Einsele, G., 2000. Coastal and shallow sea sediments. In: Sedimentary Basins Evolution, Facies, and Sediment Budget, second ed. Springer, pp. 94—153.

El Gazzar, A.M., Moustafa, A.R., Bentham, P., 2016. Structural evolution of the Abu Gharadig field area, northern Western Desert, Egypt. J. Afr. Earth Sci. 124,

340—354. https://doi.org/10.1016/j.jafrearsci.2016.09.027.

El Hossainy, M.M., Abdelmaksoud, A., Ali, M., Alrefaee, H.A., 2021. Integrated sedimentological and petrophysical characterization of the lower cenomanian clastic Bahariya reservoir in Abu Gharadig Basin, Western Desert, Egypt. J. Afr. Earth Sci. 184, 104380.

El-Sharkawi, M.A., Al-awadi, S.A., 1982. Alteration products of glauconite in burgan oil field, Kuwait. J. Sediment. Petrol. 52, 999—1002.

EREX, 2015. Biostratigraphy and Lithostratigraphy of NEAG 2-4St Well (Unpublished results).

Fahmy, M., Mostafa, M.M., Darwish, M., Saber, S., 2018. Geological framework of jurassic sequences, east tiba sub-basin, North Western Desert, Egypt. Egypt. J. Geol. 62, 53—69.

Fahmy, M., Mostafa, M., Darwish, M., El-Araby, A., 2023. Implementations core properties and sedimentary facies on the reservoir quality of the lower cenomanian upper Bahariya member in East Abu El-Gharadig Basin, Western Desert, Egypt. J. Afr. Earth Sci. 105106. https://doi.org/10.1016/j.jafrearsci.2023.105106.

Farouk, S., Sen, S., Ganguli, S.S., Abuseda, H., Debnath, A., 2021. Petrophysical assessment and permeability modeling utilizing core data and machine learning approaches — a study from the Badr El Din-1 field, Egypt. Mar. Petrol. Geol. 133, 105265. https://doi.org/10.1016/j.marpetgeo.2021.105265.

Farrag, G.H., Baghdady, A., Elnaggar, O.M., 2021. Petrophysical attributes of the middle zone of the Bahariya Formation as a producing reservoir using core analysis correlations and log evaluation, Abu Sennan area, Egypt. J. Afr. Earth Sci. 180, 104225. https://doi.org/10.1016/j.jafrearsci.2021.104225.

Gradstein, F.M., Ogg, J.G., Schmitz, M., Ogg, G., 2012. The Geologic Time Scale, first ed. Elsevier BV.

Halliburton, 2011. NEAG C-5E-1 Oil Mud Reservoir Imager Log Interpretation Report (Unpublished results).

Halliburton, 2015. BAPETCO NEAG 2-4St Well X-Tended Range Micro-imager (XRMI) Report (Unpublished results).

Hartmann, D.J., Beaumont, E.A., 1999. Predicting reservoir system quality and performance. In: Foster, N.H., Beaumont, E.A. (Eds.), Exploring for Oil and Gas Traps. AAPG, pp. 461—617. https://doi.org/10.1306/TrHbk624C9.

Hassan, S., Tahoun, S.S., Darwish, M., Bosworth, W., Radwan, A.E., 2023. The albian-cenomanian boundary on the southern tethyan margin: Abu Gharadig Basin, northern Western Desert, Egypt. Mar. Petrol. Geol. 154, 106334. https://doi.org/10.1016/j.marpetgeo.2023.106334.

Jafarian, A., Kakemem, U., Husinec, A., Mehrabi, H., Javanbakht, M., Wang, C., Li, Y., 2024. Depositional facies and diagenetic control on reservoir quality of the Aptian Dariyan Formation, NW Persian Gulf. Mar. Petrol. Geol. 106895. https://doi.org/10.1016/j.marpetgeo.2024.106895Getrightsandcontent.

Javier, O., Lagraba, P., Hansen, S.M., Spalburg, M., Helmy, M., 2010. Borehole image tool design, value of information, and tool selection. In: Poppelreiter, M., Garcia-Carballido, C., Kraaijveld, M. (Eds.), Dipmeter and Borehole Image Log Technology: AAPG Memoir, vol. 92. AAPG, pp. 15—38. https://doi.org/10.1306/13181275M923403.

Krause, F.F., Collins, H.N., Nelson, D.A., Machemer, S.D., French, P.R., 1987. Multiscale anatomy of a reservoir: geological characterization of pembina-cardium pool, west-central alberta, Canada. AAPG (Am. Assoc. Pet. Geol.) Bull. 71, 1233—1260. https://doi.org/10.1306/703c8051-1707-11d7-8645000102c1865d.

Li, Y., Bhattacharya, J., 2014. Facies architecture of asymmetrical branching distributary channels: Cretaceous Ferron Sandstone. Sedimentol. Utah 61, 1452—1483. https://doi.org/10.1111/sed.12104.

Martín-Chivelet, J., Fregenal-Martínez, M.A., Chacón, B., 2008. Traction structures in contourites. In: Rebesco, M., Camerlenghi, A. (Eds.), Developments in Sedimentology, vol. 60. Elsevier B.V., pp. 159—182. https://doi.org/10.1016/S0070-4571(08)10010-3

Mattioni, L., Chauveau, A., Fonta, O., Ryabchenko, V., Sokolov, E., Mukhametzyanov, R., Shlionkin, S., Zereninov, V., Bobb, I., 2010. A 3-D fracture model of the Kuyumba oil field (eastern Siberia) reflecting the clay and bed thickness-related fracture-density variations of its dolomite reservoir. In: Poppelreiter, M., Garcia-Carballido, C., Kraaijveld, M. (Eds.), Dipmeter and Borehole Image Log Technology, vol. 92. AAPG Memoir, pp. 211—227. https://doi.org/10.1306/13181285M923404.

Mehrabi, H., Esrafili-Dizaji, B., Hajikazemi, E., Noori, B., Mohammad-Rezaei, H., 2019. Reservoir characterization of the burgan Formation in northwestern Persian gulf. J. Petrol. Sci. Eng. 174, 328—350. https://doi.org/10.1016/j.petrol.2018.11.030.

Nelson, R.A., 1985. Geologic Analysis of Fractured Reservoirs: Contributions in Petroleum Geology and Engineering. Gulf Publishing Company, Houston.

Nichols, G., 2009. Sedimentology and Stratigraphy, second ed. Wiley-Blackwell.

Odin, G.S., Matter, A., 1981. Glauconite origin. Sedimentology 28, 611—641.

Pontén, A., Plink-Björklund, P., 2009. Regressive to transgressive transits reflected in tidal bars, Middle Devonian Baltic Basin. Sediment. Geol. 220 (3—4), 48—60. https://doi.org/10.1016/j.sedgeo.2009.04.003.

Prelicz, R.M., Fearfield, D., Sobera, M., Roeterink, R., Van der Harst, C., 2014. Identifying New Opportunities through Reservoir Performance Reviews and Systematic Benchmarking of TQ Recovery. Society of Petroleum Engineers. https://doi.org/10.2118/172095-MS.

Rashad, O., El-Barkooky, A.N., El-Araby, A., El-Tonbary, M., 2022. Deterministic and stochastic seismic inversion techniques towards a better prediction for the reservoir distribution in NEAG-2 field, north Western Desert, Egypt. Egypt. J. Petrol. 31, 15—23. https://doi.org/10.1016/j.ejpe.2021.12.002.

Rogers, S.J., Fang, J.H., Karr, C.L., Stanley, D.A., 1992. Determination of lithology from

well logs using neural network. AAPG (Am. Assoc. Pet. Geol.) Bull. 76, 731−739. https://doi.org/10.1306/BDFF88BC-1718-11D7-8645000102C1865D.

Rumelhart, D.E., Hintont, G.E., Williams, R.J., 1986. Learning representations by back-propagating errors. Nature 323, 533−536. https://doi.org/10.1016/B978-0-323-60984-5.00062-7.

Said, S.G., Tahoun, S.S., Galal, T.R., Effat, N.K., 2021. Successive first downhole sporomorph-events: applied biostratigraphic tool for fault delineation within baharyia formation, Abu sennan area, Abu Gharadig Basin, Egypt. J. Afr. Earth Sci. 175, 104095. https://doi.org/10.1016/j.jafrearsci.2020.104095.

Samantray, A., Kraaijveld, M., Bulushi, W., Spring, L., 2010. Interpretation and application of borehole image logs in a new generation of reservoir models for a cluster of fields in Southern Oman. In: Poppelreiter, M., Garcia-Carballido, C., Kraaijveld, M. (Eds.), Dipmeter and Borehole Image Log Technology, vol. 92. AAPG Memoir, pp. 343−357. https://doi.org/10.1306/13181292M923413.

Sarhan, M.A., Collier, R.E.L., 2018. Distinguishing rift-Related from inversion-related anticlines: observations from the Abu Gharadig and gindi basins, Western Desert, Egypt. J. Afr. Earth Sci. 145, 234−245. https://doi.org/10.1016/j.jafrearsci.2018.06.004.

Schatzinger, R.A., Tomutsa, L., 1999. Multiscale heterogeneity characterization of tidal channel, tidal delta, and foreshore facies, Almond formation outcrops, rock springs uplift, Wyoming. In: Schatzinger, R., Jordan, J. (Eds.), Reservoir Characterization-Recent Advances, vol. 71. AAPG Memoir, pp. 45−56. https://doi.org/10.1306/m711c4.

Schlumberger, 1995. Geology of Egypt. In: Nurmi, R., Perrin, P., Robertson, D., Coates, J. (Eds.), The Well Evaluation Conference. Schlumberger, pp. 15−33.

Schlumberger, 2015a. NEAG 2-5 Full-Structural and Sedimentological Analysis, FMI Report (Unpublished results).

Schlumberger, 2015b. Bapetco Multiwell (NEAG2-5, NEAG2-4ST1, and NEAGC5E-1) Stratigraphic Correlation Report (Unpublished results).

SENV, 2008. NEAG Extension Concession Exploration Well Proposal (Issue Report No. EP200802258396) (Internal report).

SENV, 2009. Biostratigraphic Study for Well NEAG C5- 1 (Unpublished results) (Issue June).

Shehata, A.A., Sarhan, M.A., 2022. Seismic interpretation and hydrocarbon assessment of the post-rift cenomanian Bahariya reservoir, Beni Suef basin, Egypt. J. Pet. Explor. Prod. Technol. 12, 3243−3261. https://doi.org/10.1007/s13202-022-01520-2.

Shehata, A.A., El Fawal, F.M., Ito, M., Abdel Aal, M.H., Sarhan, M.A., 2018. Sequence stratigraphic evolution of the Syn-Rift early cretaceous sediments, west Beni Suef basin, the Western Desert of Egypt with remarks on its hydrocarbon accumulations. Arabian J. Geosci. 11, 1−18. https://doi.org/10.1007/s12517-018-3688-y.

Shi, X., Cui, Y., Xu, W., Zhang, J., Guan, Y., 2020. Formation permeability evaluation and productivity prediction based on mobility from pressure measurement while drilling. Petrol. Explor. Dev. 47, 146−153. https://doi.org/10.1016/S1876-3804(20)60013-1.

Slatt, R.M., 2006. Stratigraphic Reservoir Characterisation for Petroleum Geologists, Geophysicists, and Engineers. Elsevier.

Stearman, M., 2023. Interdisciplinary approach to reservoir surveillance in the levant basin. Mediterranean Gas Exploration Symposium, Innovations for the Next Zohr. El Alamin City, Egypt.

Tesseir, B., 2012. Stratigraphy of tide-dominated estuaries. In: Davis, R.A., Dalrymple, R.W. (Eds.), Principles of Tidal Sedimentology. Springer, Netherlands, pp. 109−128.

Ulmer-Scholle, D.S., Scholle, P.A., Schieber, J., Raine, R.J., 2016. A Colour Guide to the Petrography of Sandstones, Siltstones, Shales and Associated Rocks, vol. 109. AAPG Memoir.

Wahdan, M., Fahmy, M., Brekelmans, H., 1996. 3D reservoir modelling and simulation in BAPETCO: case studies from the BED 1, 2 and 3 fields, Western Desert, Egypt. Proceedings 13th Petroleum Conference, pp. 250−260.

Worden, R.H., Morad, S., 2003. Clay Minerals in Sandstones: Controls on Formation, Distribution and Evolution, vol. 34. The International Association of Sedimentologists special publication. Blackwell Publishing, pp. 3−41. https://doi.org/10.1002/9781444304336.ch1.